2007

Composite left-handed materials and negative refraction in photonic crystals

Lei Zhang
Iowa State University

Composite left-handed materials and negative refraction in photonic crystals

by

Lei Zhang

A dissertation submitted to the graduate faculty
in partial fulfillment of the requirements for the degree of
DOCTOR OF PHILOSOPHY

Major: Electrical Engineering

Program of Study Committee:
Gary Tuttle, Co-major Professor
Costas M. Soukoulis, Co-major Professor
Rana Biswas
Jiming Song
Robert Weber

Iowa State University
Ames, Iowa
2007

TABLE OF CONTENTS

LIST OF FIGURES

ACKNOWLEDGEMENTS

Foremost, I would like to thank my advisors Prof. Costas Soukoulis and Prof. Gary Tuttle for providing me with the opportunity to complete my PhD thesis at the Iowa State University. I am very grateful for their immense theoretical and experimental knowledge, constant inspiration and guidance, patience, encouragement, enthusiasm, and financial support. Without their support and mentoring, this thesis would not have been possible. I am deeply indebted to them.

I would also like to express my sincere gratitude to Prof. Rana Biswas, Prof. Jiming Song, and Prof. Robert Weber for serving on my Ph.D. examination committee. I have benefited greatly from courses that I have taken from Prof. Biswas and Prof. Weber, and discussions with Prof. Song.

In the course of this thesis, my current and former colleagues and friends at Iowa State University have helped me kindly with their expertise in various aspect of research. Specifically, I thank Dr. Thomas Koschny for answering patiently many questions that I have encountered. I thank Dr. Stavroula Foteinopoulou for helping me get familiarized in the field of left-handed materials. A thank you to my lab mate Jiangfeng Zhou, who has been kind in sharing with me simulation programs, and engaging in many productive discussions. I would like to thank Dr. Rabia Moussa for collaborating with me in several research projects. I also thank Dr. Curtis Sell in the Microwave laboratory of the Microelectronics Research Center for initially introducing me to the facilities in the laboratory.

Part of the research projects in this thesis were carried out in collaboration with

Phantom Works of the Boeing company. I would like to thank its members for the pleasant collaboration, especially Dr. Minas Tanielian, Dr. Claudio Parazzoli, and Dr. Robert Greegor. It is also my pleasure to extend my gratitude to Prof. Ekmel Ozbay at the Bilkent University in Turkey for our fruitful collaborations.

Last but not least, I thank my family for their unfailing support.

ABSTRACT

The field of left-handed materials has drawn growing attention due to their novel and unique electromagnetic (EM) properties. Left-handed materials are composite materials with simultaneous negative dielectric permittivity ϵ and negative magnetic permeability μ. Electromagnetic waves are left-handed in left-handed materials and the unique properties of such materials lead to a collection of remarkable phenomena, some of which have been theoretically predicted and experimentally observed by many research groups in the past few years. The research of left-handed materials has had and will continue to have significant impacts on the fields of physics, optics and engineering.

In this dissertation we start from a brief review of this exciting new field, covering from the early history to the recent investigations of metamaterials as well as negative refraction phenomena in photonic crystals. Following the steps of history, we presents the theoretical works back from the 1960's, then the realization of left-handed materials, and the experimental verifications by a number of research groups, including the first left-handed metamaterial composed of arrays of wires and SRRs in the year of 2000 and some most recent designs. Some of the interesting phenomena, namely negative refraction and perfect lensing are also mentioned in the first chapter. Negative refraction phenomena in photonic band gap structures is described here as well.

We next proceed in Chapter 2 to analyze the interaction between the components of split ring resonator (SRR) and wires in left-handed materials. An effective way to check the left-handedness of the composed metamaterials is presented and explained. SRRs are the more complicated component in the conventional left-handed metamaterials.

How propagation and polarization direction of incident electromagnetic waves affect the behavior of SRRs is also investigated here with both numerical and experimental results. It is concluded in Chapter 2 that SRRs show different EM responses for different polarization and propagation directions of incident electric field due to the anisotropy of the SRR's geometry. A simple review of how to retrieve electromagnetic parameters from transmission and reflection coefficients is described at the end of this chapter to explicate the procedure we used to obtain permittivity and permeability from scattering parameters.

In Chapter 3, we present an isotropic design of polarization independent SRRs. Ideas for achieving extremely small inherent size SRRs are proposed and verified numerically and experimentally. Comparisons of the new designs are also presented. An interesting project — how to control the behavior of SRRs/wires structures is briefly discussed at the end.

Chapter 4 investigates negative refraction phenomena and superlensing effect in two different two-dimensional photonic crystal structures. Transmission properties of two-dimensional photonic crystal structures composed of dielectric materials are obtained and analyzed. Results from theoretical and experimental studies are reported and they confirm the observing of left-handed behavior in the photonic crystals we proposed.

Finally in Chapter 5 several experimental methods involved in the course of the measurements to verify the negative refractive index of left-handed materials are presented. We demonstrated how to obtain transmission and reflection coefficients that can be used to retrieve electromagnetic parameters. Determination of the refractive index of testing materials by measuring the location of first node of standing wave is also described.

CHAPTER 1 Background of Left-Handed Materials

Recently, left-handed materials (LHM), also addressed as negative index material (NIM), have attracted a great deal of attention due to their novel and unique physical properties. In this chapter we present a brief review of this exciting new field, covering from the early history to the recent investigations of metamaterials as well as negative refraction phenomena in photonic crystals.

1.1 Early hypothesis and prediction of left-handed materials

Existing materials in nature transparent to electromagnetic radiation that we are aware of all have positive refractive index — a refractive index that is greater than zero. However, could it be possible that there are materials possessing a negative refractive index and what would be the unique properties of such materials if they do exist? V. Veselago first investigated this question and theoretically conjectured the electromagnetic properties of media with simultaneously negative electric permittivity ϵ and negative magnetic permeability μ [48].

In Veselago's paper, the propagation of electromagnetic waves in a substance with $\epsilon < 0$ and $\mu < 0$ was studied by looking into Maxwell's equations. For the plane monochromatic wave solutions, in which all fields are proportional to $e^{i(k\cdot r-\omega z)}$, Maxwell's equations read:

$$\begin{aligned} k \times E &= \omega\mu\mu_0 H, \\ k \times H &= -\omega\epsilon\epsilon_0 E. \end{aligned} \tag{1.1}$$

Here, E and H are electric and magnetic field of electromagnetic wave, k the wave vector, ω the circular frequency, μ and ϵ the relative permeability and permittivity of the medium, respectively, and c the vacuum speed of light. It can be seen that when $\epsilon < 0$ and $\mu < 0$, E, H and k form a left set of vectors, see Fig. 1.1. Because of this, materials with simultaneously negative ϵ and μ are also called left-handed materials, while materials with both positive ϵ and μ, where E, H, k form a right set of vectors are called right-handed (RH) materials.

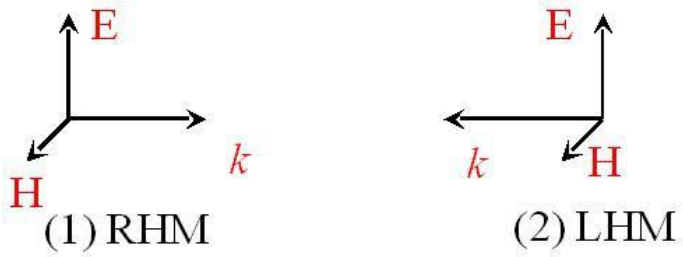

Figure 1.1 (1) If $\epsilon > 0$, $\mu > 0$, then (E, H, k) is a right set of vectors; (2) if $\epsilon < 0$, $\mu < 0$, then (E, H, k) is a left set of vectors.

In right-handed materials, (E, H, k) and (E, H, S) are both right set vectors, where S is Poynting vector, defining the directions of energy flow. Since

$$S = E \times H, \tag{1.2}$$

S does not relate to the permittivity and permeability (ϵ, μ) of the material. So in left-handed materials, S still forms a right set of vectors with the electric field E and magnetic field H. Therefore, in left-handed materials, S and k are in opposite directions, which means energy flux and phase velocity are opposite. This property brings about interesting phenomenon, such as

- reversed Doppler effect: in left-handed material a receiver moving towards the electromagnetic radiation source will perceive a lower frequency than that of the source.

- negative refraction
- reversed Cherenkov effect

The connection between frequency ω and wave vector for a plane wave solution is given by dispersion equation. In the case of an isotropic material, the dispersion relation is written as:

$$k^2 = \frac{\omega^2}{c^2}\epsilon\mu, \tag{1.3}$$

It can be seen that when the real part of the product of $\epsilon\mu$ is positive, the wave can propagate in the medium, see Fig. 1.2. The region in the first quadrant is where the permittivity and permeability are both positive. Most known materials in nature fall in this region and they have been the most explored. Plasma falls in the second quadrant, a plasma is typically an ionized gas where electrons in the atom are separated from nucleus. Metals is also considered metals plasma below plasma frequency. However, the remaining part of the map has not been explored as much. This is because materials are not so easily available in these regions. In fact, materials that lie in the third quadrant, where the permittivity and permeability are both negative, do not appear in nature at all.

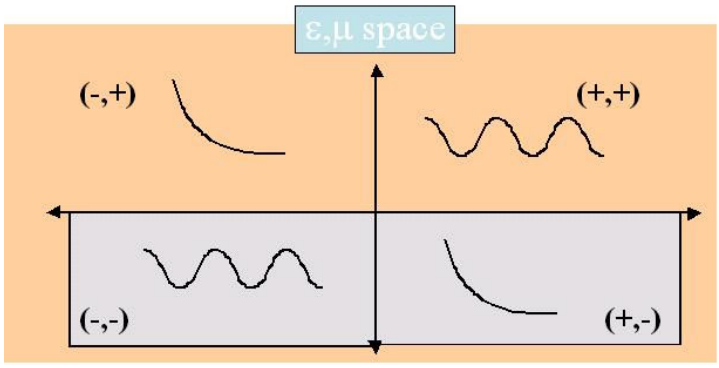

Figure 1.2 (ϵ, μ) space. Propagating waves occur in the first and third quadrants; waves are not able to travel in the second and forth quadrants.

In Veselago's paper, it is also concluded that simultaneous negative value of ϵ and μ can only be realized when there is frequency dispersion. When there is no frequency dispersion nor absorption, the total energy density is:

$$W = \epsilon E^2 + \mu H^2, \tag{1.4}$$

When ϵ and μ are both negative, the total energy density would be negative as well, which is physically impossible. When there is frequency dispersion, the relation of (1.4) is modified as:

$$W = \frac{\partial(\epsilon\omega)}{\partial\omega} E^2 + \frac{\partial(\mu\omega)}{\partial\omega} H^2, \tag{1.5}$$

A more general description of electromagnetic energy density in dispersive and absorptive materials can be found in Ref [38]. A positive energy density is only guaranteed if

$$\frac{\partial(\epsilon\omega)}{\partial(\omega)} > 0, \frac{\partial(\mu\omega)}{\partial(\omega)} > 0, \tag{1.6}$$

Therefore, left-handed materials must always be dispersive.

1.2 Negative refraction and Superlensing

Electric permittivity ϵ and magnetic permeability μ are medium parameters used to describe how medium polarize interacting with light and other electromagnetic fields. They are related to refractive index as follows:

$$n = \pm\sqrt{\epsilon\mu} \tag{1.7}$$

The sign of the index is commonly taken as positive, as in all known natural materials. Nevertheless Veselago pointed out that if a medium has both negative permittivity ϵ and

negative permeability μ, the sign must be reversed.

This reversal of the sign of the refractive index has stimulated a lot of confusion and debate. For example, the velocity of an electromagnetic wave in a medium is written as c/n, where c is the speed of light in vacuum. When the refractive index is negative, does it mean that the wave travels backwards? Actually the definition of c/n is the phase velocity and depict the speed at which wave maxima travel through a fixed point in the medium. As addressed before, the phase velocity in negative index material is opposite to the energy velocity. So when a wave packet travels in left-handed material, the envelope moves away from source as energy velocity's direction is flowing away from source; however the phase front travel backwards as phase velocity is directed back to the source, see Fig. 1.3.

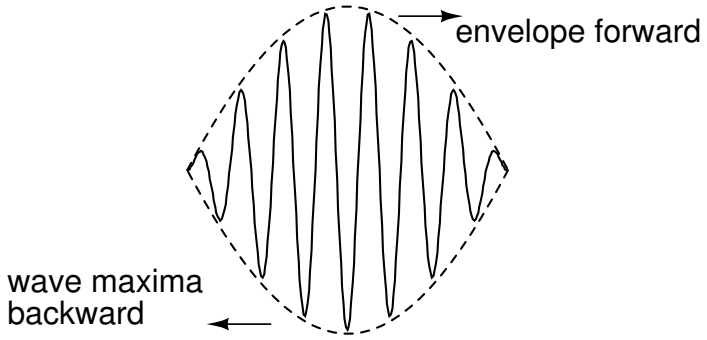

Figure 1.3 Wave packet traveling in negative index material

The refractive index also determines the deflection of a beam as it enters or leaves the interface to the medium at an angle. Snell's law states the quantitative relation between the angle of incidence, transmission and refractive index:

$$n_1 \sin(\theta_1) = n_2 \sin(\theta_2), \tag{1.8}$$

For a beam entering from right-handed medium to left handed medium, since n_2 is negative, the deflected beam is at the same side of the normal, see Fig. 1.4. As a result the angle of transmission is "negative" and the refraction at the interface of RH/LH is

called "negative refraction".

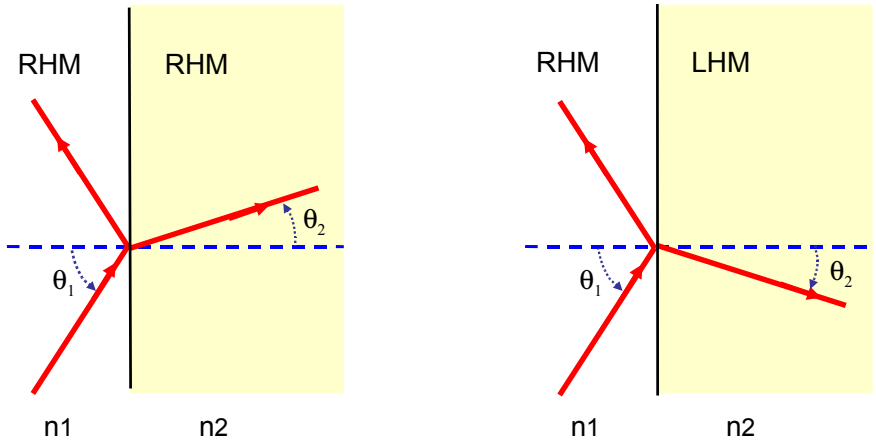

Figure 1.4 "Reversal of Snell's law": refraction between RH/RH and RH/LH medium

Negative refraction bends rays of light in a reversed way and thus has a focusing effect. Actually J. B. Pendry proposed that a slab of negative index material could work as perfect lens [33], see Fig. 1.5. Besides the perfect lens could bend propagating waves, evanescent waves could also contribute the imaging, beyond the usual diffraction limit.

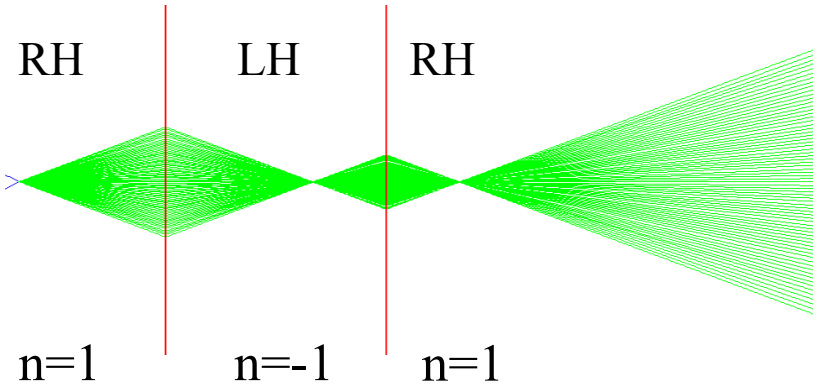

Figure 1.5 Planar slab of negative material focuses rays of light from a point source

We know the finer details of the electromagnetic near fields are evanescent and do not propagate, normal optical lenses can not focus evanescent waves and have a resolu-

tion limit: only propagating waves can be focused by a normal lens and contribute to the image; the evanescent waves are lost. The maximum resolution is of the order of wavelength and sub-wavelength imaging can not be realized by normal optical materials. However, for a planar slab of negative index material with $\epsilon, \mu = -1$ and no losses, a perfect image exists that carries all the information of the source at the opposite side of the slab. It is shown that evanescent waves can be amplified exponentially by the lossless negative index material, while in normal medium it decays exponentially, see Fig. 1.6. The idea of perfect lens was criticized by several research groups [13, 11]. Losses in negative index material lead to a new limitation of the perfect lens resolution. In addition, It was argued that only when the electromagnetic source is put very close to the NIM slab, sub-wavelength imaging could be possible [36]. Moreover, due to the dispersive property of left-handed materials, the slab lens can only focus for a narrow region of frequencies. Still, negative index slab provides a new way of manipulating lights and electromagnetic waves.

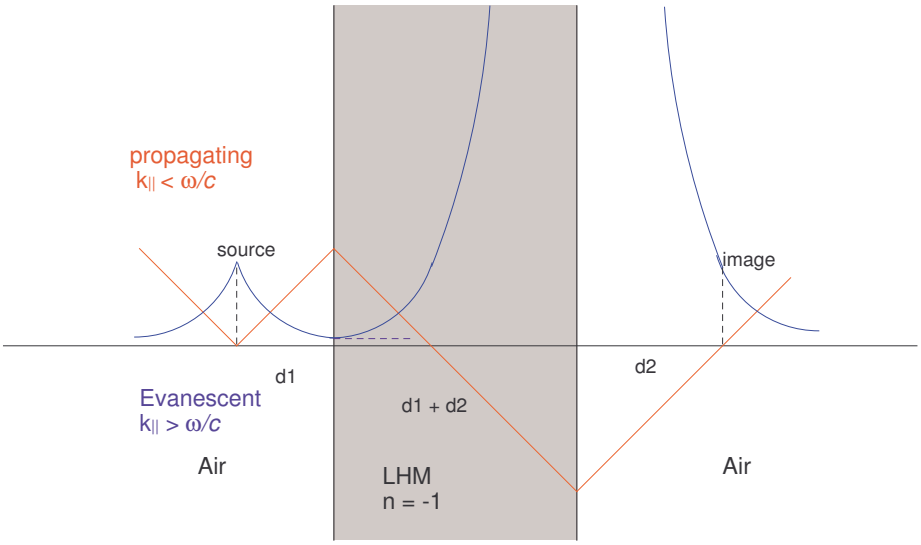

Figure 1.6 Propagating waves and evanescent waves focus through a perfect lens

Negative index materials manipulate electromagnetic wave in such unconventional

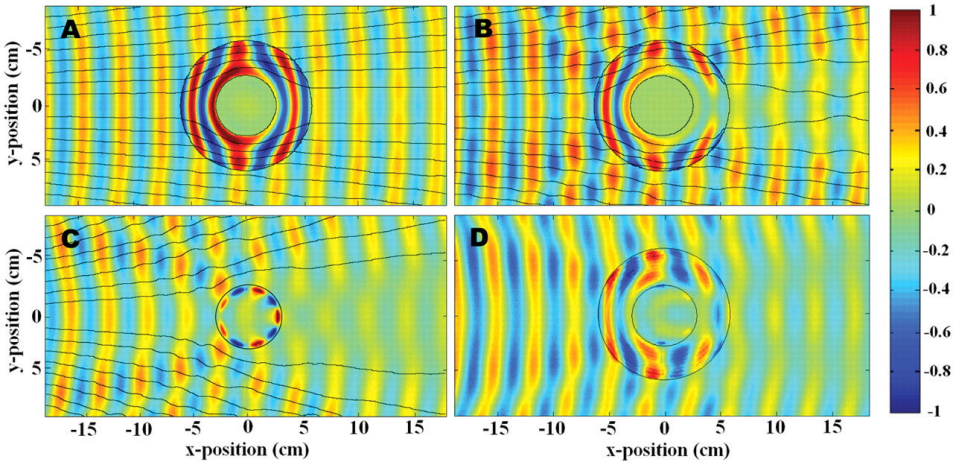

Figure 1.7 Snapshots of time-dependent, steady-state electric field patterns, with stream lines [black lines in (A to C)] indicating the direction of power flow (i.e., the Poynting vector). The cloak lies in the annular region between the black circles and surrounds a conducting Cu cylinder at the inner radius. The fields shown are (A) the simulation of the cloak with the exact material properties, (B) the simulation of the cloak with the reduced material properties, (C) the experimental measurement of the bare conducting cylinder, and (D) the experimental measurement of the cloaked conducting cylinder. Animations of the simulations and the measurements (movies S1 to S5) show details of the field propagation characteristics within the cloak that cannot be inferred from these static frames. The right-hand scale indicates the instantaneous value of the field [39]

way. Depending on negative refraction, cloaking effects may be realized through NIM's ability to influence the direction of light that passes through it. Recently researchers have shown that a cloak of invisibility is in principle possible, at least over a narrow frequency band. In Ref. [39] the first practical realization of such a cloak was presented. The cloak was constructed with the use of artificially structured metamaterials, designed for operation over a band of microwave frequencies. The cloak decreased scattering from the hidden object inside while at the same time reducing its shadow, so that the cloak and object combined began to resemble empty space, see Fig. 1.7.

1.3 Realization of left-handed materials

Although the idea of left-handed materials was proposed almost fifty years ago, the realization of such material was not implemented until recently. It was demonstrated that composite material composed of artificial resonant structures can show effective negative ϵ and μ. In this section, we present why left-handed materials can be regarded as homogeneous medium, and review a sequence of events that enabled the realization of LHM.

1.3.1 Effective Medium

As we mentioned above, dielectric permittivity and magnetic permeability are commonly used parameters to describe how locally homogeneous materials polarize under the effects of an electric field and magnetic field. From the electromagnetic point of view, when the wavelength of the electromagnetic wave is a lot larger then the size of atoms or molecules, the wave would not "see" the tiny details but rather some averaged response. For example, when light is incident on a piece of glass, the wavelength of light(around 500nm) is hundreds times larger than the atomic level(usually several angstroms). So the atomic details of glass are no longer important in depicting how the glass interact with light. In that case the glass is considered uniform and can be characterized by effective macroscopic electromagnetic parameters ϵ and μ. These two parameters can be determined by the scattering properties, see ref [37].

For the artificial NIM consisting natural materials such like metal or/and dielectric, if the wavelength of incident electromagnetic wave is much larger than the unit cell size of NIM structure, NIM can be regarded as a homogeneous material as well. Although NIM is inhomogeneous, the electromagnetic waves interacting with the structure at the frequencies of interest can not tell the difference.

1.3.2 Low Frequency Plasmon and Magnetic Resonators

In 1996, Pendry et al [34] demonstrated a periodic array of thin metallic wires to possess a plasmon-like dielectric permittivity as given in (1.9). This composite structure is constituted of infinitely long thin wires in square lattice, see Fig. 1.8.

$$\begin{aligned} \epsilon_{eff} &= \epsilon_\infty[1 - \frac{\omega_p^2}{\omega(\omega + i\Gamma)}], \\ \omega_p^2 &= \frac{2\pi c^2}{d^2 \ln d/r}, \Gamma = \frac{d^2\omega_p^2\epsilon_0}{\pi r^2 \sigma} \end{aligned} \tag{1.9}$$

Here ω_p is the effective plasmon frequency, Γ is the plasma collision frequency. They can be calculated from the parameters of the wire array. d is the lattice of wire array, r is the radius of wire and σ is the conductivity of the metal. At frequencies below ω_p, the wire array shows electromagnetic properties of a negative permittivity material.

We can see immediately that (1.9) takes the same form as dielectric function of metal bulk material. Actually we could consider the thin wire array as diluted metal bulk material, but the thin wire array has much lower plasmon frequency (in microwave regime) then natural metal material (usually in ultraviolet regime).

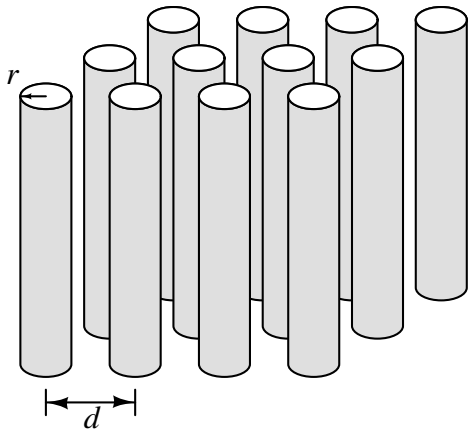

Figure 1.8 Conducting wire array makes effective negative permittivity medium

The structure of an artificial magnetic resonator was proposed in the year of 1999 [35]. The magnetic resonator usually has the shape of a split-ring or Swiss-roll, see Fig. 1.9. Essentially it is a inductor-capacitor resonator circuit, the metallic ring itself has inductance and the gap introduces capacitance. For frequencies below or far above resonance, the effective μ is positive; near resonance, the responding magnetic momentum is opposite to the incident magnetic field and this translates to negative permeability.

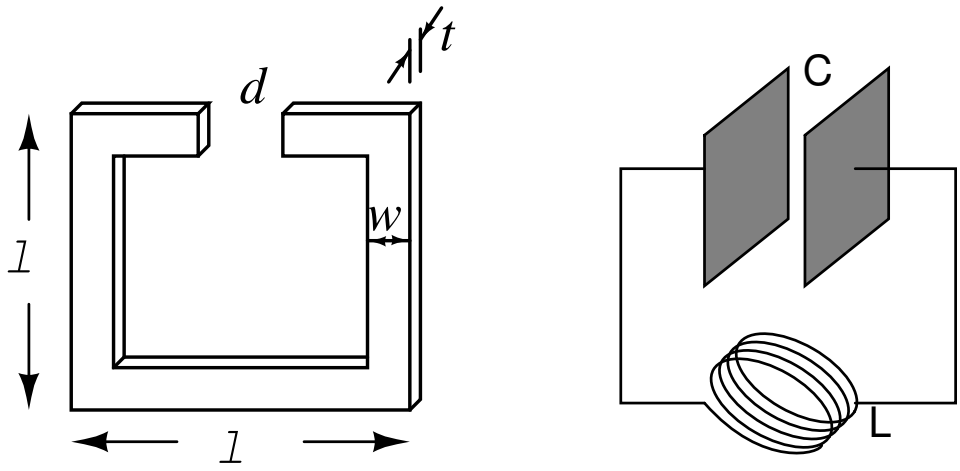

Figure 1.9 Split-ring resonator and its equivalent circuit

It was demonstrated that arrays of ring resonators could respond to the magnetic component of incident radiation, displaying an effective permeability. The effective permeability of ring resonator was given by Pendry [35] as:

$$\begin{aligned} \mu_{eff} &= \mu_\infty[1 - \frac{F\omega^2}{\omega^2 - \omega_0^2 + i\Gamma_m\omega)}], \\ F &= \frac{\pi R^2}{d^2}, \\ \omega_0^2 &= \frac{3dc^2}{\pi^2 R^3 \ln(r_w/h)}, \\ \Gamma_m &= \frac{dc^2}{2\pi R\sigma}, \end{aligned} \tag{1.10}$$

where d is period of the structure, R is the radius of the resonator, r_w is the radius of the wires, h is the distance between rings in SRR, σ is the conductivity of the metal material. A plot of the effective permeability for an ideal SRR over frequency is shown in Fig. 1.10.

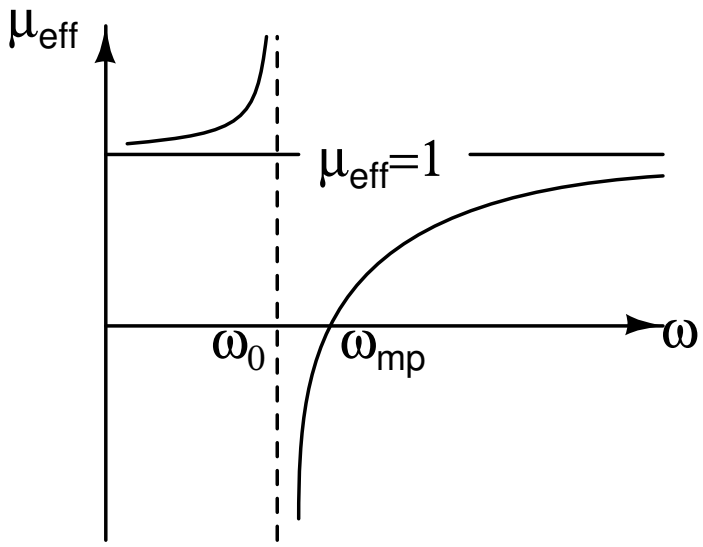

Figure 1.10 Spectrum of effective magnetic permeability of SRR

1.3.3 First left-handed material and its verification

In 2000, D. R. Smith and his collaborators fabricated the first composite structure that constituted a negative index material operating at microwave frequencies [43]. One of such structure is shown in Fig. 1.11, consisting of alternating layers of wires and slit-ring resonators. Smith also experimentally tested that the LHM structure exhibit properties of LHM, such like negative refraction. Later on, more experimental demonstrations of LHM have been reported [43, 41, 40, 2, 32, 1]. Recently metamaterials at telecommunication and visible frequencies has been fabricated and tested[6].

In ref [43], It was demonstrated that the one-dimensional left-handed material structure (wire array combined with SRR array) has a transmission band at a narrow band

Figure 1.11 First composite structure of wire array and SRR array [43]

of frequencies where the wire array or SRR array individually show a band gap. Transmission experiments of two dimensional structure was performed as well.

Along with transmission experiments, negative index of refraction was also measured in prism shaped metamaterial. A diagram of how negative refraction experiment have been set up is shown as Fig. 1.12.

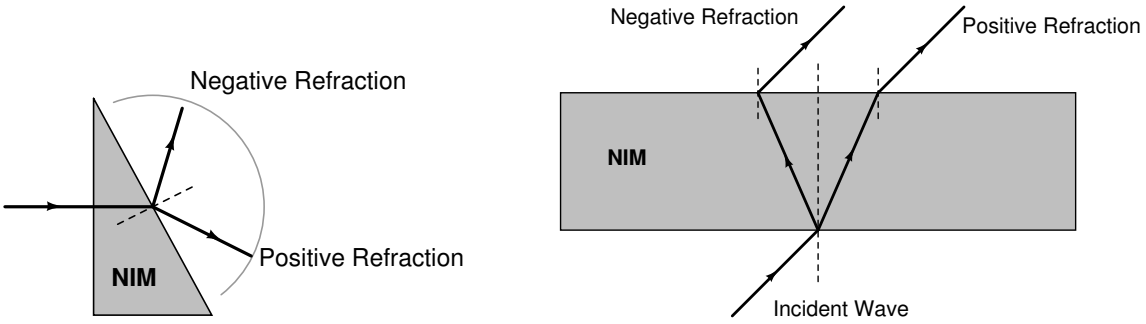

Figure 1.12 Negative refraction experiment scheme

Most reported NIMs have combined non-resonant wires to realize the electric response and conducting split ring resonators to realize the magnetic response. Continuous wires is a very simple design, however realization of negative permittivity by the use of continuous wires also has disadvantages. The effective plasma frequency (and frequency band of negative permittivity) is lowered as the unit cell size increases, making NIM

metamaterials with unit cell dimensions much smaller than the wavelength problematic. Alternatively, arrays of finite length wires can be used to create negative permittivity metamaterials. When cuts are present in the wires periodically, the capacitive gap between wires introduces a resonance. Instead of exhibiting negative permittivity at all frequencies below cutoff like continuous wires, cut wires shows a band of negative permittivity between a lower resonance frequency and an upper cutoff frequency. The resonance frequency is significantly dependent on the capacitance of the gap between the wires, also making the cut wire lattice difficult to design accurately.

Recently, Ruopeng Liu et al. [22] have demonstrated a relatively broadband NIM which makes use of SRRs and a new type of electric resonators, tuned such that they resonate at the same frequency and with nearly the same frequency dispersion. The NIM properties are confirmed by direct measurements of the phase variation and field distributions, obtained by field mapping. Fig. 1.13 shows the SRR and electric LC resonator used to construct the negative index metamaterials.

The electric LC resonators can be regarded as combination of two identical SRRs placed back-to-back.When excited by an electric field, currents flow in such a manner that resonant magnetic response is canceled out, leaving only a resonant electric response. ELCs are convenient to control and can be made relatively insensitive to the cell-to-cell coupling. Experimental results in the microwave regime are also reported in [22].

Besides experimental efforts, a lot of numerical studies was confirmed by plenty of researcher groups, e.g., to obtain scattering parameters by simulating a unit cell of the composite structure and retrieve effective permittivity and permeability from reflection and transmission coefficients [46, 24, 26, 7, 25, 27, 44, 18]. There are several effective numerical simulation methods, including finite-difference time-domain (FDTD), finite-difference frequency-domain (FDFD), scattering matrix, modified transfer-matrix method [26], as well as commercial simulation packages, such as CST Microwave Studio,

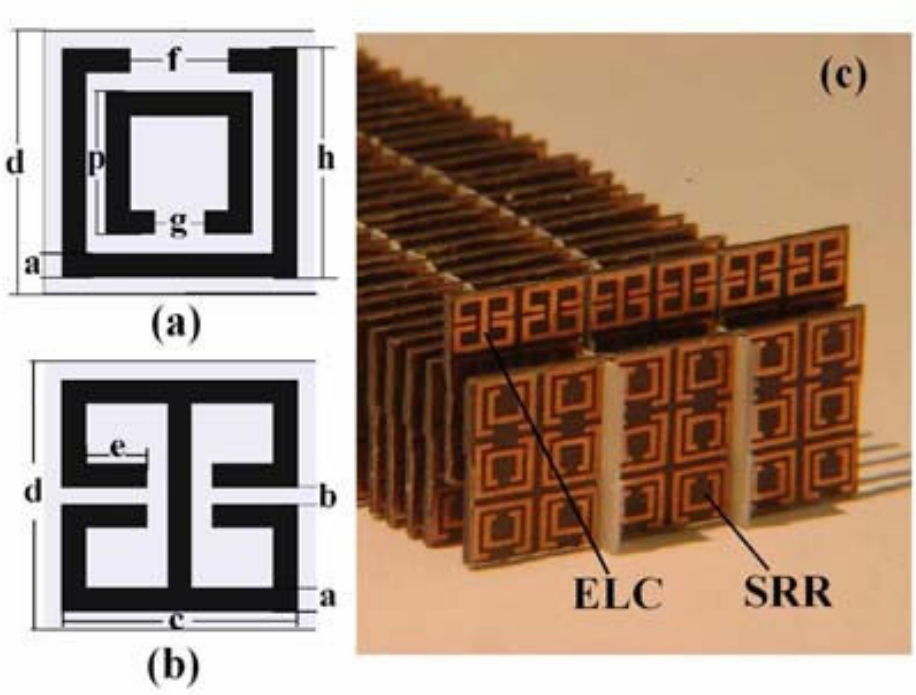

Figure 1.13 (a) SRR structure, (b) ELC structure, (c) Picture of SRR-ELC NIM sample [22]

Ansoft High Frequency Simulation Software, and Comsol Multiphysics.

1.4 Negative Refraction in Photonic Crystals

Photonic crystals are media where the dielectric function is periodically modulated. They are designed to mold and control the flow of light like the way semiconductor controls electrons. Photonic crystals have certain frequency regions that no electromagnetic waves can propagate inside in any direction. The frequency regions that allow no propagation are called photonic band gaps. Thanks to this valuable property, photonic crystals can be utilized in the application of waveguide, antennas, laser devices, etc.

The phenomenon of negative refraction was also discovered and verified in photonic crystals [29, 23, 5]. In 1998 a hexagonal 3D photonic crystal composed of alternating layers of S_i and S_iO_2 was found for which small deviation of incident angle results in

a huge deviation of the transmission angle. Furthermore, for all angles of incidence, incident beam and transmission beam are at the same side to the normal, that is, the refraction is negative [16]. This phenomenon is called superprism. Negative refraction in photonic crystals enables a photonic crystal slab to work as a lens. Notomi investigated the light propagation in a strongly modulated two dimensional photonic crystal and predicted negative refraction could occur at a frequency region where the dispersion relation is almost isotropic [29]. Moreover Luo et al studied negative refraction behavior of a photonic crystal for a frequency region around the band edge of the first band for a photonic crystal of square lattice [23]. Cubukcu et al verified experimentally single-beam negative refraction and demonstrated superlensing effect in the valence band of 2D photonic crystal similar to the system in Ref. [23] operating in microwave regime.

Negative refraction can be both observed in left-handed material and photonic crystals. However photonic crystals do not have negative refractive index. We know that left-handed and PC are both composed of periodically arranged structures. For left-handed material, the propagating electromagnetic wavelength is much larger than the lattice of unit structure; but for photonic crystals, the wavelength is comparable with the period of the structure. So effective medium theory does not apply to photonic crystals. It is not possible to define a physically meaningful effective permeability and permittivity by retrieving the transmission and reflection coefficients of a photonic crystal.

The negative refraction phenomena in PC was theoretically explained using the equifrequency surface (EFS) [29]. The equifrequency surface is a surface that contains all allowed wave vector within the first Brillouin zone for a certain frequency, analogue to the Fermi surface in semiconductor field. A very simple case of EFS is given here, see Fig. 1.14. The EFS of homogeneous NIM and air are the red and black circle. At the boundary the tangential component of the wave vector is conserved, so that the wave vector could be pointed towards point A or B. Since the direction of energy flow must point away from the source, in NIM only the wave vector pointed to A corresponds to a

Poynting vector away from the source - at the negative side of the surface normal. The EFS of photonic crystal is a lot more complicated than the homogeneous case.

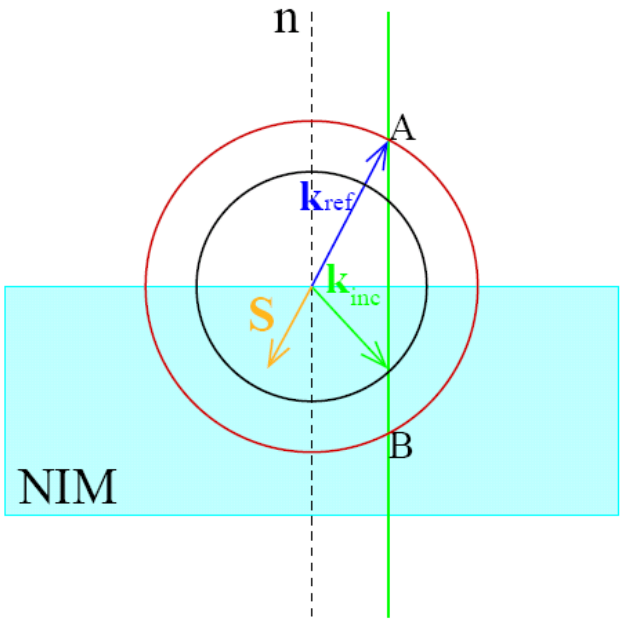

Figure 1.14 Negative refraction at the surface NIM with circular EFS and air[10]

Foteinopoulou et al demonstrated a two-dimensional PC system in which S and k are almost opposite to each other. This case resembles a uniform negative index material [7]. Foteinopoulou et al also use FDTD simulation method to study the time evolution of an EM wave as it hits the interface of air and the PC system. The wave is trapped temporarily at the interface, reorganizes, and, after a long time, the wave front moves eventually in the negative direction. This particular example shows how causality and speed of light are not violated in spite of the negative refraction always present in a negative index material.

1.5 Summary

The research of left-handed materials has had a significant impact on the field of physics, optics and engineering. It offers opportunities to make artificial metamaterials that has unique electromagnetic properties which are impossible to find in conventional, naturally existing materials. The ability to manipulate the value of the permittivity or permeability opened many new possibilities in different fields of physics and engineering. Superlensing, cloaking etc are possible application of the novel metamaterials. Nowadays materials with effective ϵ and effective μ or effective refraction index near zero have also become the subject of investigation [42], one of the application of such near zero metamaterials is electromagnetic tunneling, for example. As we move forward, we believe left-handed metamaterials and related metamaterials can lead us to more novel applications and dramatic physical phenomena.

CHAPTER 2 Electromagnetic Response of LHM

SRRs and wires shows magnetic and electric response to an incident electromagnetic wave. While their individual response has been discussed in the previous chapter, in this chapter we will analyze interaction between the component of SRR and wires in LH materials. How propagation and polarization direction affect the behavior of SRRs will also be investigated here.

2.1 Electric response of SRR

Since the original microwave experiment of Smith et al., several LHMs were fabricated [43, 32] that exhibited a pass band in which it was assumed that ϵ and μ are both negative. This assumption was based on transmission measurements of the wires alone, the split ring resonators(SRR) alone, and the LHMs. The occurrence of a LHM transmission peak within the stop bands of the SRR and wire structures was taken as evidence for the appearance of LH behavior. Further support to this interpretation was provided by the demonstration that such LHMs exhibit negative refraction of EM waves [41, 14]. Moreover, there is a significant amount of numerical work [26, 25, 27, 31] in which the transmission and reflection data are calculated for a finite length of metamaterial. A retrieval procedure can then be applied to obtain the macroscopic electromagnetic parameters ϵ and μ under the assumption that it can be treated as homogeneous. This procedure was applied in Ref. [44] and confirmed that a medium composed of SRRs and wires could indeed be characterized by effective ϵ and μ whose real parts were both negative over a finite frequency band, as was the real part of the refractive index n.

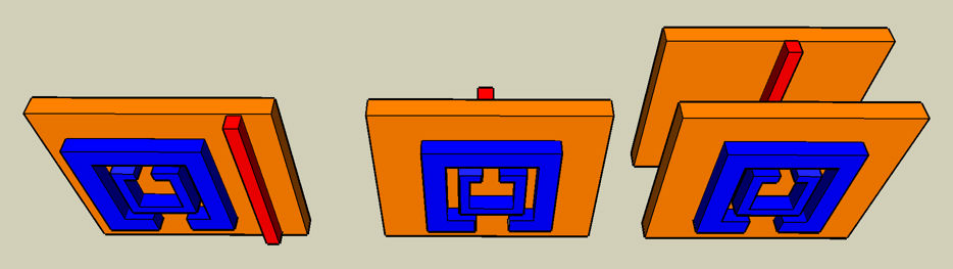

I II III

Figure 2.1 Different geometries of LHM combined SRRs and wires

However, it was later shown [15] that the SRRs exhibit a resonant electric response in addition to their resonant magnetic response, and, therefore, make the understanding and the fabrication of true LHMs more challenging.

The conventional LHM could combines SRRs and wires in different configurations, like shown in Fig. 2.1. SRRs and wires can be attached to opposite side of dielectric board on which they stand; or SRRs and wires are constructed on the same side of standing board; moreover, SRRs and wires can also be fabricated on separate boards and placed together in alternating layers.

In all those different combination cases, there are non-negligible interactions between the SRRs and wires. We noticed that the effective plasma frequency of LHM is considerably lower than the one of wire arrays alone . This effect is due to that SRRs have magnetic response as well as electric response. As seen in Fig. 2.2, the composite metamaterial (CMM) is periodical stacking of SRRs boards and wires boards, like type II in Fig. 2.1. The measured transmission peak is actually a right-handed peak [2]. Due to the additional response of SRRs, the effective plasma frequency of the composite structure is moved to lower region, which may possibly be even a slightly lower than the magnetic resonance frequency of SRRs. At this region both effective electric permittivity and magnetic permeability are positive.

A simple and effective way to study the combined electric response of SRRs and wires is to destroy the magnetic response of SRRs without interfering the electric response. We

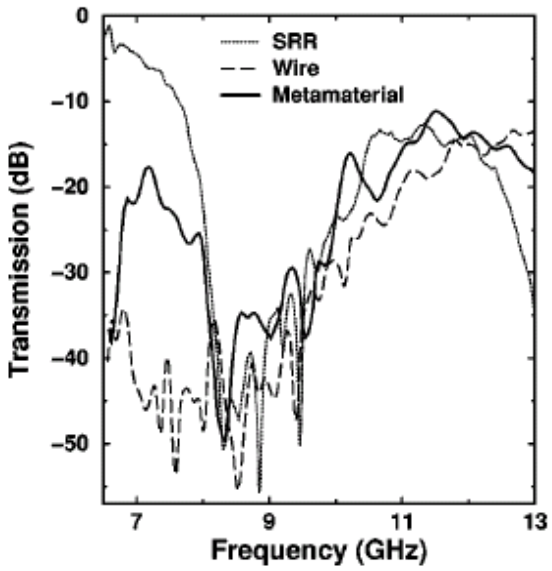

Figure 2.2 Measured transmission spectra of thin wires, SRRs and the composite structure. The transmission passband is actually a right-handed peak although it appears where both SRRs and wires has stop band alone [2].

know the exclusive source of magnetic response of LHM is the circulating current in the SRR, which is equivalent to the oscillating current in a Inductor-Capacitor resonator circuit. By closing the gap of the SRR, the magnetic resonance is annihilated since the capacitor is destroyed; at the same time, this alteration to electric response can be assumed to be small because only a very small portion of metal is added.

In the following we will present a CMM consisting of a periodically arranged SRRs and wires structures. The work has been reported in [1]. The magnetic resonance of the SRR structure will be demonstrated by comparing the transmission spectra of SRRs with those of closed SRRs. Simulation results show that the effective plasma frequency of the LH material composed of SRRs and wires is lower than the plasma frequency of the wires.

The SRR and Closed SRR (cf. Fig. 2.3) units are fabricated on a FR4 circuit board with a deposited copper layer of 30-μm thickness. The geometric parameters of the SRR are $d = t = 0.2mm$, $w = 0.9mm$, and $r = 1.6mm$. The circuit board has a 1.6 mm thickness and dielectric constant $\epsilon = 4.4$. The dimensions of a unit cell containing a single SRR are $a_x = a_y = 8.8mm$ and $a_z = 6.5mm$.

Fig. 2.4 shows the simulated transmission spectra of periodic SRRs and closed SRRs from 3 to 14 GHz. The first bandgap of the SRR medium is not present in the closed SRR medium, indicating that it belongs to the magnetic resonance providing $\mu < 0$. The second bandgap is present for both the SRR medium and the closed SRR medium. This simulation clearly shows that the stop bands of a SRR medium cannot be assumed to be purely negative μ behavior. Higher frequency region of the observed gaps could originate from the electrical response of the SRRs or from Bragg gaps that are due to periodicity [19]. Experiment measurement has been done by K. Aydin et al and the simulation results agrees extremely well with measurement data.

As we pointed out earlier, the SRRs exhibit resonant magnetic response as well as electric response. This behavior due to electric character is similar to that of a periodic

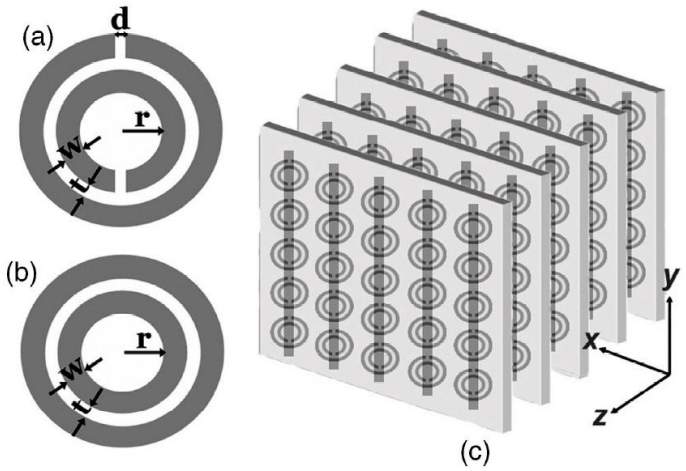

Figure 2.3 Schematics of (a) a single SRR, (b) a Closed SRR, (c) a periodic metamaterial composed of SRRs on one side and wires on the other side of a dielectric board.

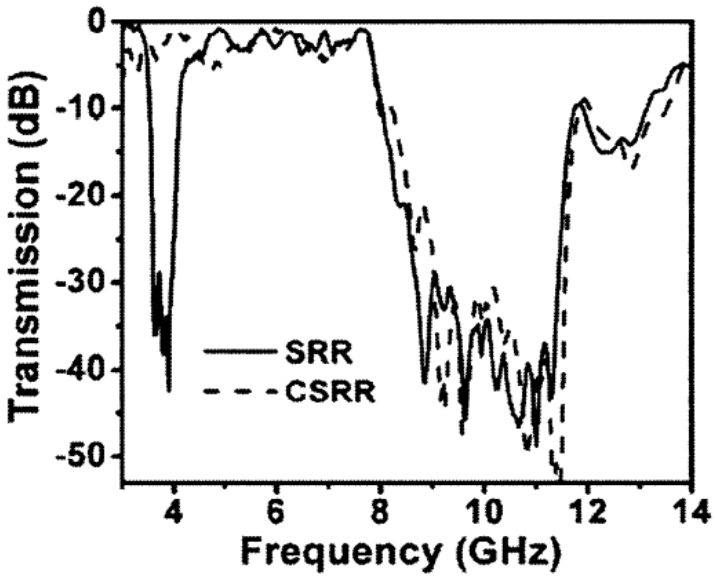

Figure 2.4 Simulated transmission spectra of a periodic SRR medium and a periodic closed SRR medium from 2 to 14 GHz.

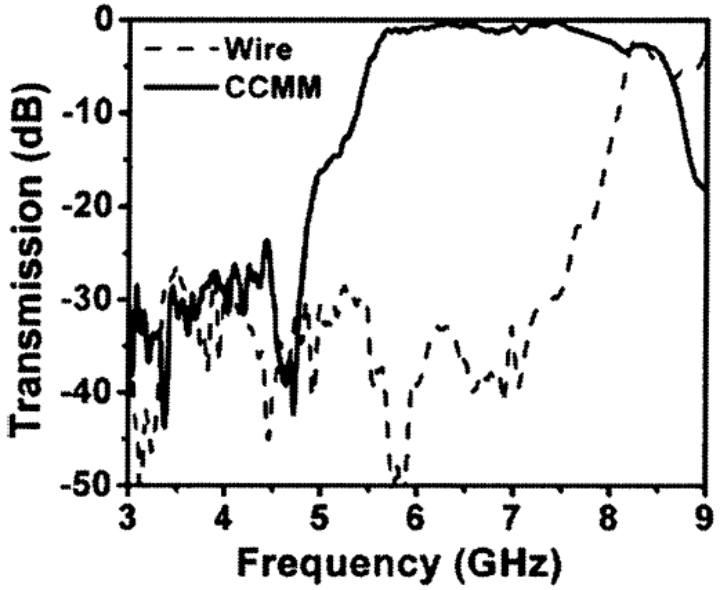

Figure 2.5 Transmission spectra of wires and CMM with closed SRRs

cut-wire medium which has a stop band with a lower edge that is due to the discontinuous wire geometry [30]. As a result, the SRRs contribute to the effective permittivity of the CMM, shifting the plasma frequency to lower region. Simulation has been done to compare the effective plasma frequency of wires only and of a metamaterial consisting of periodic alternating layers of closed SRRs and wires Fig. 2.5. If the effective plasma frequency is even lower than the magnetic resonance frequency, a right-handed peak will be observed.

Both simulation and experiment show that the effective plasma frequency is higher than the magnetic frequency, which guarantees the left-hand property of the CMM's transmission peak appearing around at 4GHz. The transmission spectra of SRR only, wire only, and CMM periodic structures are displayed in Fig. 2.6.

From above, we can see a well-defined LH transmission band with a high peak value is obtained. The experimental results agree extremely well with the theoretical calculations by MWS. The left-handed transmission band exactly coincides with the region where

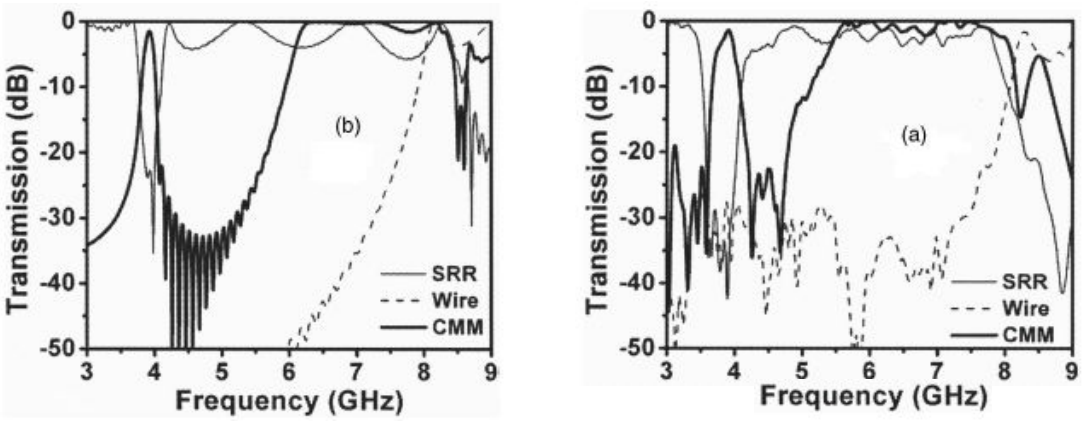

Figure 2.6 Transmission spectra of wires and CMM with closed SRRs

both dielectric permittivity and magnetic permeability take negative values.

2.2 Electric coupling to the magnetic resonance

We have learned that the SRRs have a considerable electric response in addition to magnetic response. In that case, we assumed that the only source of magnetic resonance is the induced circulating current flowing in the SRRs coupling to the external magnetic field that is perpendicular to the plane of SRRs. Based on this assumption, it would be impossible to observe transmission gap at magnetic resonance frequency when the external magnetic field is in the plane of SRRs, since no induced oscillating current would be generated. However, simulation and experiment results showed that a strong transmission gap around the magnetic resonance frequency are observed in some cases even when the applied magnetic field is the plane of the SRRs.

There are several different configurations of the directions of wave propagation and E field polarization respect to the plane of SRRs, they are shown in Fig. 2.7.

In the following, we present numerical and experimental results for the transmission coefficient of a lattice of SRRs for the different orientations shown in Fig. 2.7. This work was reported in [50]. It was considered an obvious fact that an incident EM wave excites

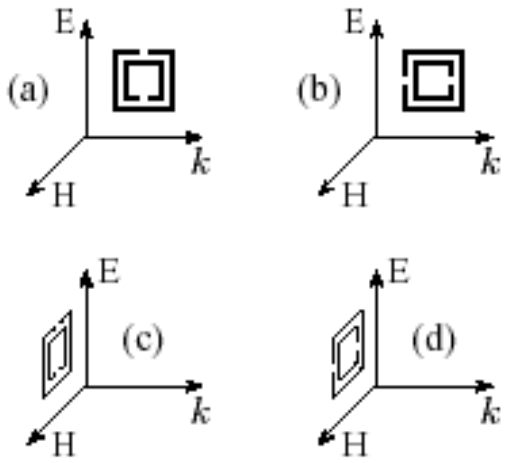

Figure 2.7 Different orientations of the SRR with respect to the external electric field E and the direction of propagation

the magnetic resonance of the SRR only through its magnetic field; hence, the magnetic resonance response appears only if the external magnetic field H is perpendicular to the SRR plane(Fig. 2.7 [a] and Fig. 2.7 [b]), which, in turn, implies a direction of propagation k parallel to the SRR plane. If H is parallel to the SRR, no coupling to the magnetic resonance was expected.

However, if the direction of propagation is perpendicular to the SRR plane and the incident E is parallel to the sides of the SRRs which contain the cuts (Fig. 2.7 [d]), we observed an electric coupling of the incident EM wave to the magnetic resonance of the SRR. Similar results were obtained by others for other cases of metamaterials [15, 12]. Experiments, as well as numerical results based on the Microwave Studio, reveal that for propagation perpendicular to the SRR plane a dip in the transmission spectrum close to the magnetic resonance of the SRR appears whenever the electric field is parallel to the sides of the SRR where the gaps exist.

For the experimental study, a metamaterial consisting of SRRs was fabricated, using a conventional printed circuit board process with 10 μm thick copper patterns on one

side of a 0.254 mm thick rexolite dielectric substrate. The rexolite board has a dielectric constant of 2.53 and a dissipation factor of 0.0009 (ϵ''/ϵ') at 1.5 GHz. The design and dimensions of the SRR are almost the same as those described in [20] and quite similar to those in [40]. The geometrical parameters of the SRR are w = d = t = 0.33 mm and l = 3 mm [cf. Fig. 2.8a]. The metamaterial was then constructed by stacking together the SRR structures in a periodic arrangement, as shown in Fig. 2.8d. The unit cell contains one SRR (with outer and inner rings) and has the dimensions 4.33 mm (parallel to the cut side), 3.63 mm (parallel to the continuous side), and 5.0 mm (perpendicular to the board).

The transmission measurements were performed in free space on an orthorhombic metamaterial block consisting of $11 \times 14 \times 15$ unit cells, using a Hewlett-Packard 8510 network analyzer and microwave standard-gain horn antennas. We performed measurements for both propagation directions, perpendicular and parallel to the plane of SRRs.

Fig. 2.9 presents the measured transmission spectra, T, of the SRRs for the perpendicular propagation direction. The magnetic field, H, is parallel to the plane of the SRRs, and, therefore, no coupling to the magnetic resonance of the SRR is expected. However, as one can see from the dotted line in Fig. 2.9, there is a dip in the transmission spectra around the 13 GHz region. No dip is observed in the case shown as a solid line in Fig. 2.9. The only difference between the solid and the dotted lines in Fig. 2.9 is the direction of the incident electric field E. In the dotted line case of Fig. 2.9, where the dip in T is present, E is parallel to the gaps of the SRR (along the x-axis). In the solid line case of Fig. 2.9 , where there is no structure in T, E is perpendicular to the gaps of the SRRs (along the y-axis).

Our results suggest that the magnetic resonance of the SRRs can be also excited by the electric field. In the insert of Fig. 2.9, we present the numerical results, which are in good agreement with the measurements. They predict what direction of E gives a dip in transmission, as well as the frequency position of the dip. The numerical results were

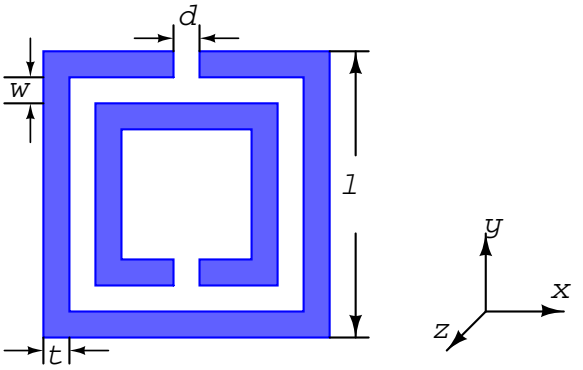

(a)

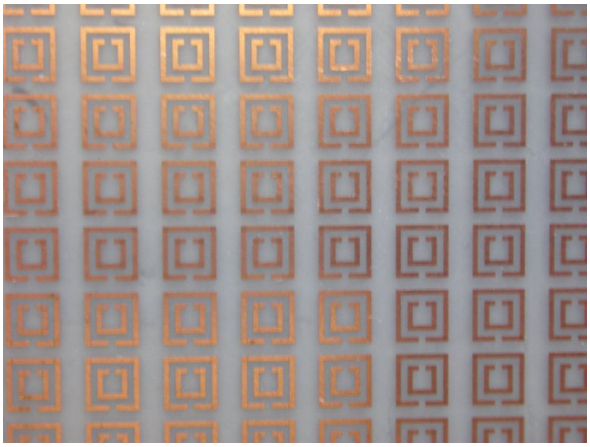

(b)

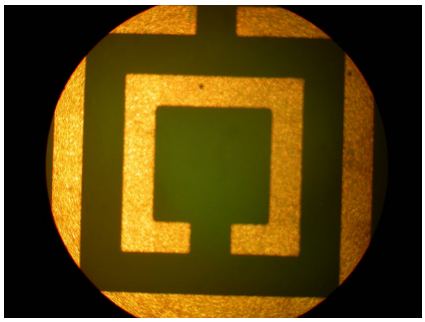

(c)

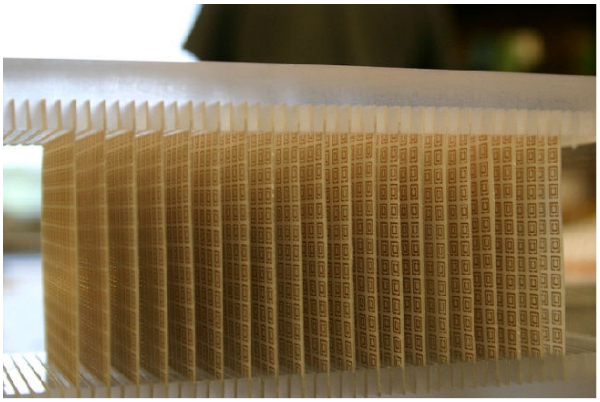

(d)

Figure 2.8 (a) The dimensions of a single SRR with w = d = t = 0.33 mm and l = 3 mm; (b)–(d) photos taken of the SRR

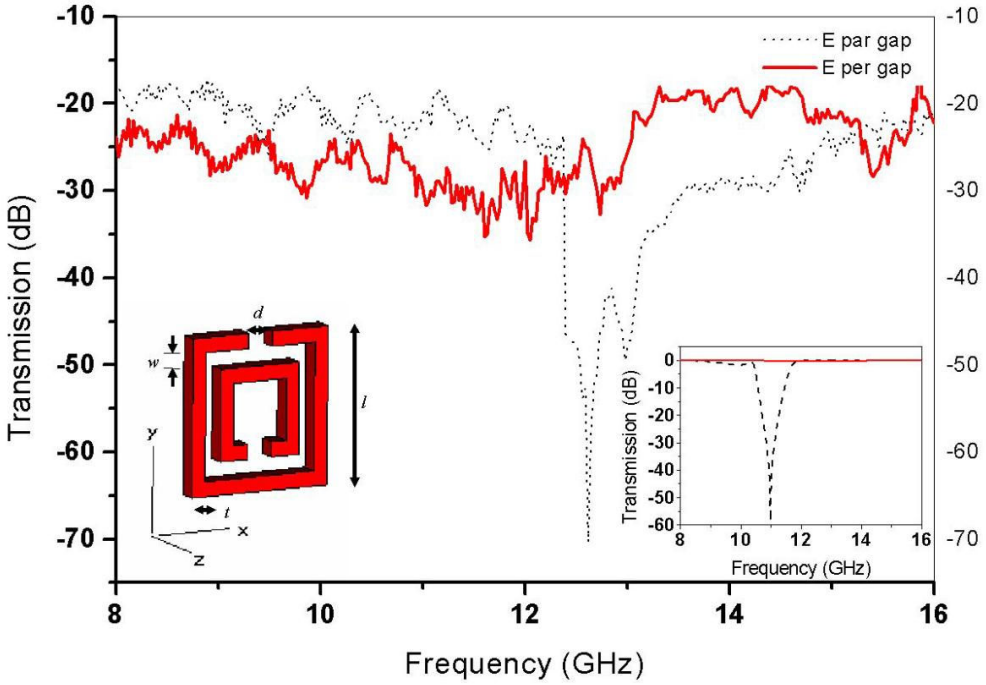

Figure 2.9 Measured transmission spectra of a lattice of SRRs for propagation direction perpendicular to the plane of SRRs (along the z-axis) for both directions of the electric field E. The solid line has E along the y-axis, while the dotted line has E along the x-axis. The inset shows the calculated transmission spectra using Microwave Studio software.

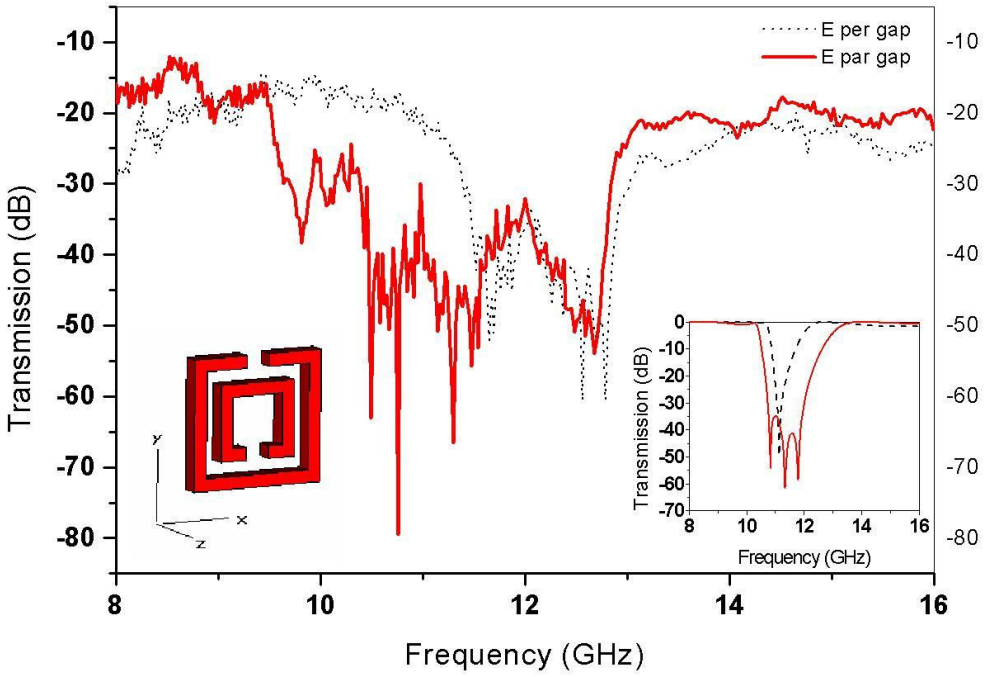

Figure 2.10 Measured transmission spectra of a lattice of SRR for propagation direction parallel to the plane of SRRs (along the x-axis) for both directions of the electric field E. The solid line has E along the y-axis, while the dotted line has E along the z-axis. The inset shows the calculated transmission spectra using Microwave Studio software.

obtained by the commercial software Microwave Studio. In our numerical analysis we only use a single unit cell in propagation direction and this is the reason for the narrower dip seen in the inset of Fig. 2.9. If more unit cells were used in the calculation, the dip will become wider, as in the experiment.

In Fig. 2.10, we present the measurements for the conventional case in the operational direction the SRR was designed for, where H is perpendicular to the SRR and the propagation direction is parallel to the plane of the SRRs. Notice that T exhibits a stop band due to the magnetic resonance of the SRR. Both the solid (E parallel to the gaps of the SRRs) and the dotted (E perpendicular to the gaps of the SRRs) lines Fig. 2.10

exhibit a stop band. In the inset of Fig. 2.10 we present the numerical results, obtained with the Microwave Studio, which are in good agreement with the measurements. We have, therefore, demonstrated both experimentally and numerically that the magnetic resonance of the SRR can be also excited by the electric field, provided that E is parallel to the gaps of the SRRs. If one closes the gaps of the SRRs [17], the dips seen in Fig. 2.9 and Fig. 2.10 disappear, which means that the dips in T are due to the magnetic response of the SRRs.

In Fig. 2.11, we present the magnitude of the magnetic field, obtained with the Microwave Studio, for the cases presented in Fig. 2.9. The frequency is 12.64 GHz, exactly at the position of the transmission dip. In Fig. 2.11(a), E is parallel to the gaps of the SRRs. One clearly sees a circular current of magnetic resonance is excited. This is due to the asymmetry of the SRRs' geometry with respect to the incident electric field, which leads to different polarizations on the arms of the SRR, one with the gap while the other without. The asymmetric polarization then amounts to an effective circular polarization current which drives the magnetic resonance. It can only occur when the electric filed of the incident wave is in-plane of the SRR and there is an asymmetry of the SRR with respect to the direction of the electric field.

In Fig. 2.11(b), E is perpendicular to the gaps of the SRRs. In this case the polarization current only flows up and down symmetrically in both sides of the SRRs. Hence no circular current appears, no coupling to the magnetic resonance of the SRR is noted, and no dip in the transmission spectra is seen because the SRR is symmetric with respect to the applied electric field. Marques et al. considered bianisotropy in SRR structures and developed an analytical model to evaluate the magnitude of cross-polarization effects [28].

In Fig. 2.12, we present the results for effective values of the electrical permittivity ϵ and the magnetic permeability μ obtained by our retrieval procedure [18], as we will mention in the next section. In Fig. 2.12a, the propagation direction is perpendicular

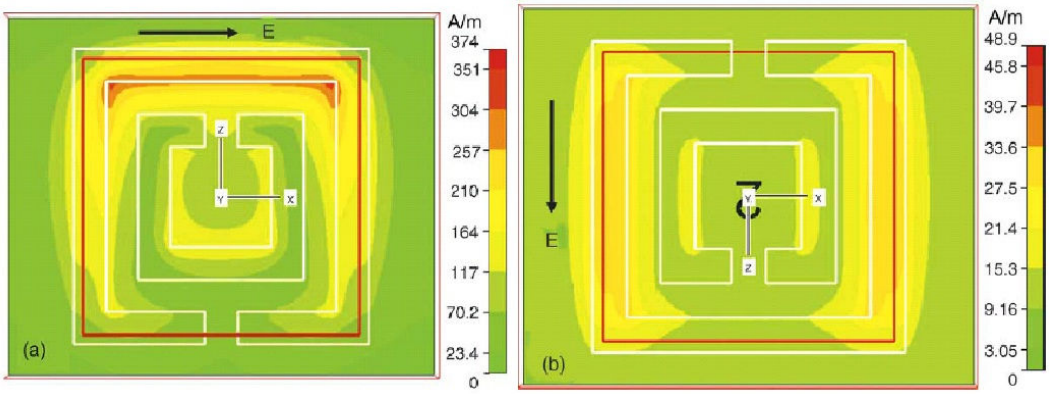

Figure 2.11 The H field in two different orientations of a single ring SRR, as obtained by Microwave Studio. For both cases, the propagation direction is perpendicular to the plane of SRRs. (a) The external electric field points along the x-axis, parallel to the sides of the SRRs which contain the cuts. In this case a circular current is present, which can excite the magnetic resonance of the SRR. (b) The external field is parallel to the sides of the SRRs without cuts (along the z-axis). For this direction no circular current is generated, only a field along the sides of the SRR that does not have gaps, but has a non zero current. Therefore, no coupling to the magnetic resonance of the SRR is possible.

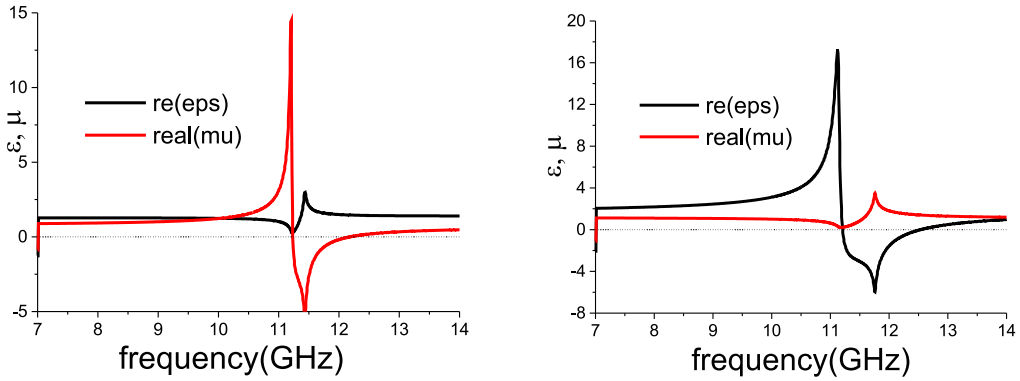

(a) (b)

Figure 2.12 The retrieval values of ϵ and μ for two different orientations of a single ring SRR, as obtained by our retrieval method [18]. (a) The propagation direction is perpendicular to the plane of the SRRs and the external electric field points parallel to the gaps of the SRR. In this case no negative μ is obtained, only the ϵ is negative. Notice that an antiresonance is obtained for the magnetic permeability μ. (b) The propagation direction is parallel to the plane of the SRRs and the external field is parallel to the gaps of the SRRs. For this direction a negative μ is generated, as expected. Notice that an antiresonance is obtained for the electrical permittivity ϵ.

to the plane of the SRRs, and the electric field points parallel to the gaps of the SRRs. In this case the retrieval procedure does not give a resonant magnetic response at the magnetic resonance, and no negative value of μ is obtained. Instead, there is an electric resonant response, as revealed by the negative value of ϵ. As discussed in [18], there is an anti-resonance response in μ, as clearly seen in Fig. 2.12(a). [18] suggested that the antiresonant behavior is caused by the requirement that the refractive index must be bounded in the structures which possess finite spatial periodicity. In Fig. 2.12(b), the propagation direction is parallel to the plane of the SRRs, and the electric field points parallel to the gaps of the SRRs. In this case the retrieval procedure does give a magnetic resonance response, as expected, and a negative value of μ is obtained. In this case, too, an anti-resonance response is obtained for ϵ.

2.3 Sketch of Effective Medium Parameter Retrieval

In this section we present a brief review of how to retrieve macroscopic electromagnetic parameters (dielectric permittivity and magnetic permeability) from scattering parameters (transmission and reflection, or S21 and S11). This procedure has been establish, references can be found at [37, 24, 26, 7, 25, 27, 44, 18]. When a metamaterial structure is exposed to electromagnetic radiation at wavelengths much larger than the unit cell size, the EM waves traveling through the medium can not "see" the details of the internal structure, but rather some homogeneous material. In this case, the effective material parameters ϵ and μ can be attributed to metamaterials.

We start from a homogeneous slab of the thickness d for normal incidence, see Fig. 2.13. The incident wave propagates along Z direction which is perpendicular to the surface (z=d1) of the slab. In region I, we have $n_1 = 1, z_1 = 1, k_1 = \frac{\omega}{c} = k$; in region II, $n_2 = n, z_2 = z, k_2 = \frac{\omega}{c/n} = nk$; in region III, we have $n_3 = 1, z_3 = 1, k_3 = \frac{\omega}{c} = k$.

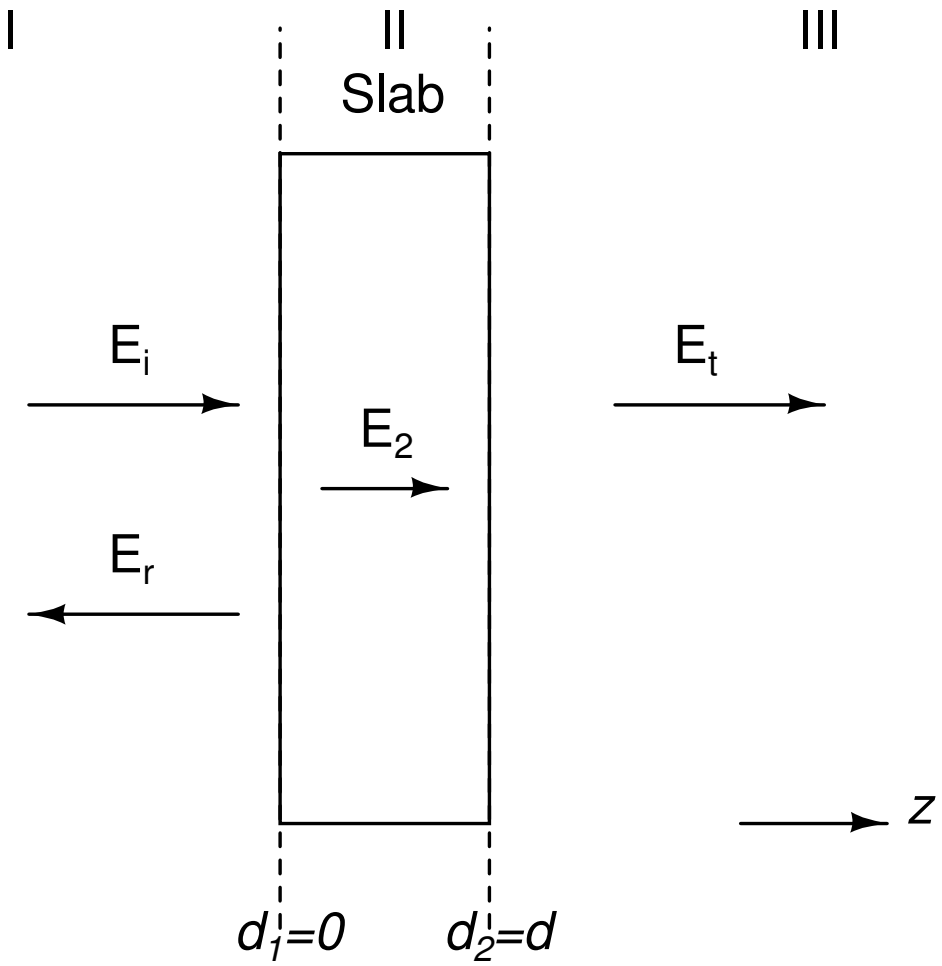

Figure 2.13 Normal incidence for a homogeneous slab

The calculated transmission and reflection coefficient are:

$$T = \frac{4z_1 z_2 e^{ik_2 d}}{(z_1+z_2)^2 - (z_1-z_2)^2 e^{2ik_2 d}} \tag{2.1}$$

$$R = \frac{(z_2^2 - z_1^2)(1-e^{2ik_2 d})}{(z_1+z_2)^2 - (z_1-z_2)^2 e^{2ik_2 d}} \tag{2.2}$$

Using the spacial properties, then we have

$$T = \left(\cos(nkd) - \frac{i}{2}\left(z + \frac{1}{z}\right)\sin(nkd)\right)^{-1} \tag{2.3}$$

$$R = -\frac{i}{2}\left(z - \frac{1}{z}\right)\sin(nkd)T \tag{2.4}$$

where both $n(k,d)$ and $z(k,d)$ are complex valued functions.

After some algebra, we find

$$\cos(nkd) = \frac{1}{2T}(1 - R^2 + T^2), \tag{2.5}$$

and

$$z^2 = \frac{(1+R)^2 - T^2}{(1-R)^2 - T^2}. \tag{2.6}$$

Solving the above equations, we get

$$z(k,d) = \pm\sqrt{\frac{(1+R)^2 - T^2}{(1-R)^2 - T^2}}, \tag{2.7}$$

$$n(k,d) = \pm\frac{1}{kd}\arccos\left(\frac{1-R^2+T^2}{2T}\right) + \frac{2\pi}{kd}m, \quad m \in \mathbf{Z}. \tag{2.8}$$

Note that the signs of z and n are not independent, fixing one for given T and R would fix the other too.

For passive materials, the impedance of the slab should satisfy:

$$Re(z) > 0 \tag{2.9}$$

or

$$Im(n) < 0 \tag{2.10}$$

The sign of z could be uniquely determined by above equations, then the sign of n can also be determined.

The permittivity ϵ and permeability μ are then obtained by:

$$\epsilon = n/z \tag{2.11}$$

$$\mu = nz \tag{2.12}$$

As shown above, the z and n obtained from the inversion of the transmission and reflection are plagued with ambiguities. From (2.7), we can see that n can be a set of values with different branches ($\frac{2\pi}{kd}m$). That n as a function of frequency is continuous can help to determine the proper branch. Some further discussion to rule out some of the possible solution can be found at [45, 37]

2.4 summary

In summary, we have shown that the magnetic component SRRs have electric response in addition to magnetic response, thus we have to consider the combination of continuous wires and SRRs as we study the effective permittivity of the composite metamaterial.

we also have presented experimental and numerical results for the propagation of EM waves for different orientations of the SRR. It is found that the incident electric field couples to the magnetic resonance of the SRR, provided its direction is parallel to

the gaps of the SRRs. There is an excellent agreement between numerical results and experiments. This unexpected electric coupling to the magnetic resonance of the SRR is of fundamental importance in understanding the transmission properties of SRRs and LHMs. This finding is very important for the design of LHMs in higher dimensions.

CHAPTER 3 Isotropic and Small Inherent Size SRR

To realize a perfect lens or for some applications, fabrication of two- or three-dimensional homogeneous and isotropic left-handed materials is required. We have demonstrated in Chapter 2 that SRRs show different EM responses for different polarization and propagation directions of incident electric field due to the anisotropy of the SRR's geometry. As a result, periodic arrangement of SRRs and wires do not yield homogeneous and isotropic left-handed materials. In this chapter, we present an isotropic design of polarization independent SRRs. How to achieve extremely small inherent size SRRs is investigated later. A very interesting project of controlling the behavior of SRRs/wires structures is briefly discussed at the end.

3.1 Opposed Rings SRR

As we mentioned earlier, SRR shows transmission dip for in-plane propagation when the electric field is parallel to the gap of SRR. A simple way to extinguish this electric coupling to magnetic resonance would be to introduce an identical gap on the other side of the SRRs, as shown in Fig. 3.1. This two-gap SRR is symmetric to the electric field and no circulating current can be generated.

By introducing the second gap, the effective capacitance of the SRR is reduced by a factor of two since the two gaps can be regarded as capacitors in series. The second gap results in higher magnetic resonance frequency since the resonance frequency depends on the effective inductance and capacitance of SRR: $\omega_m^2 = 1/(L_{eff}C_{eff})$. In this case effective medium theory may not apply because the ratio wavelength to unit cell size

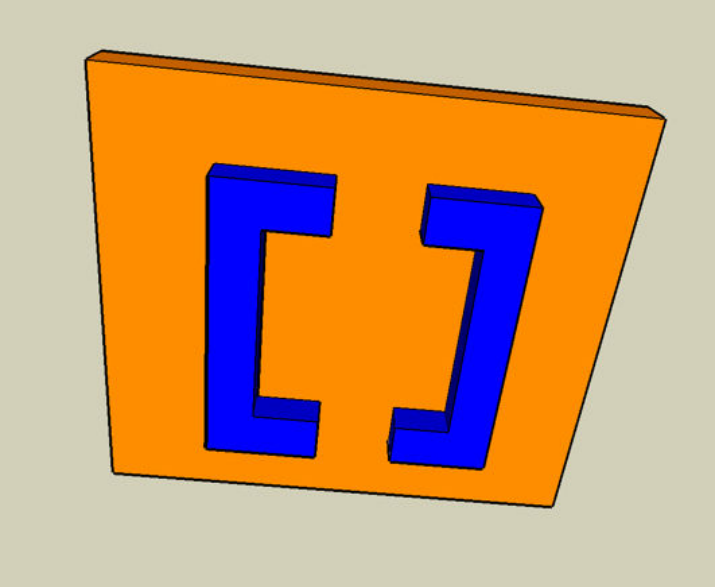

Figure 3.1 Symmetric 2-gap SRR

is reduced at the increased frequency and is no longer large enough. This problem can be prevented by increasing the gap capacities, e.g. by narrowing the gaps. However, there are very stringent limitations on the minimum gap size imposed by the fabrication process.

We propose a new design with symmetric geometric structure. The effective capacitance is preserved or even larger then the original slit ring resonator; see Fig. 3.2. Instead of adding another gap in the SRRs, an identical SRR is put on the other side of the board on which the first SRR is located. We call this structure an opposed rings resonator.

Opposed ring resonator is not absolutely symmetric in the plane of SRR. However, when the two rings are placed very closed to each other, electric coupling to magnetic resonance generated by one ring is canceled by the one opposed to it. We noticed that since the gaps of the two rings are of different size, circular current due to the broken symmetry of each SRR are of opposite directions, which leads to neutralization of electrical coupling. With reference to Fig. 3.3, we see that when the incident wave

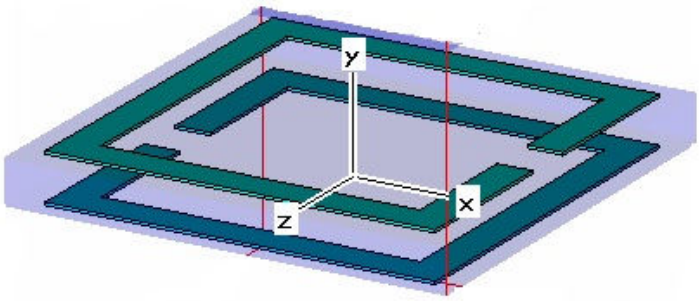

Figure 3.2 Two identical rings standing on the opposite sides of the board, the gaps are opposed to each other.

is along the plane of SRR and magnetic field is perpendicular to the SRR plane, strong resonance appears; if the incident wave is normal to the SRR plane, however, no distinct resonance is observed. The retrieved EM parameters also are plotted in Fig. 3.3.

The effectiveness of the cancellation depends on the separation between the two opposed rings. The closer the two rings are put, the less the opposed ring resonator shows electric coupling to magnetic resonance when the electric field is polarized along the gaps, see Fig. 3.4. The transmission spectrum in Fig. 3.4 is for the case where the incident Em wave is normal to the plane of SRRs and the E field is polarized along the gaps. If the separation between the two opposed ring gets closer and closer, the resonance dip flattens out and eventually vanishes.

3.2 Overleaf Capacitor SRR

Designing metamaterial elements with extremely small inherent size (about 50 or even more times smaller than their resonant wavelength) is a real challenge. Let λ denote the free space wavelength at the region of resonance, and d the characteristic size of the unit cell. For most metamaterial elements reported in the past, their $\lambda - d$ ratio is about

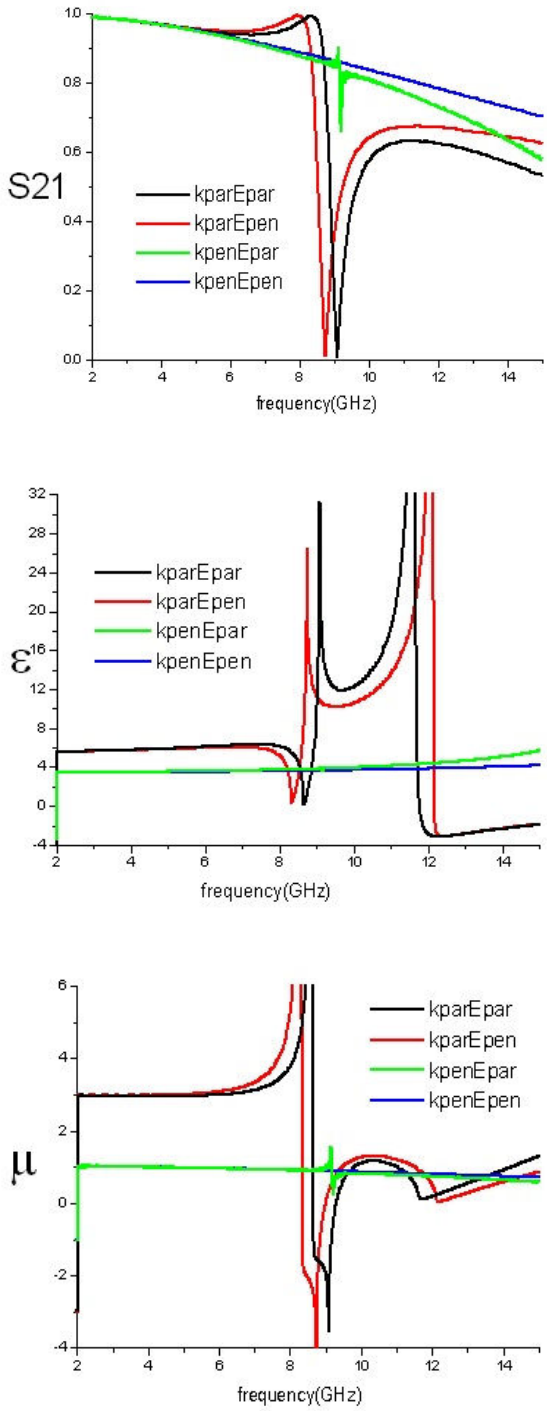

Figure 3.3 Transmission and retrieved ϵ and μ for different incident and polarization directions. kpar and kpen mean that the k vector is parallel or perpendicular to the SRR, respectively. For E field, we use Epar and Epen to distinguish, cf. Fig. 2.7.

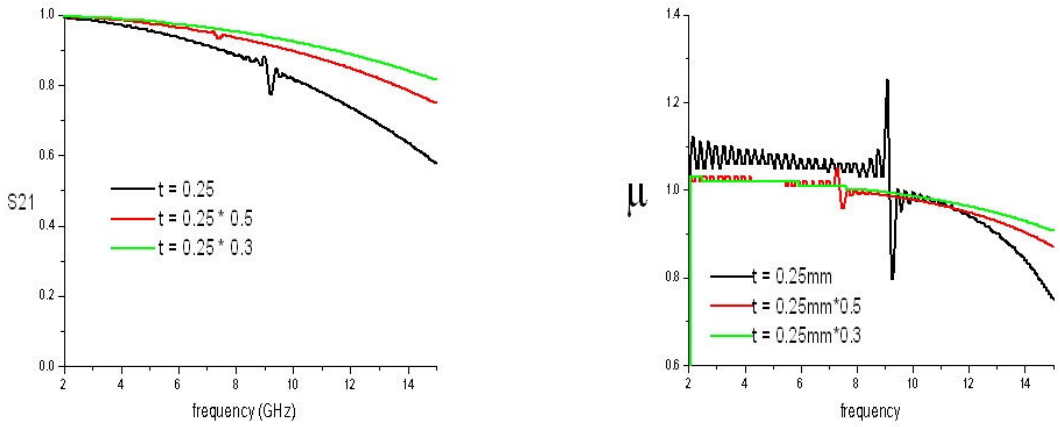

Figure 3.4 Transmission and retrieved μ of opposed ring structure for different separation between rings. t is the separation between the two opposed rings, from 0.075mm to 0.25mm

10. Surface mounted radio frequency (RF) components have been proposed to be used to increase the $\lambda - d$ ratio. For example, in order to reduce the resonant frequency for a fixed size single-ring resonator, surface mounted capacitors are soldered in the gaps, see Fig. 3.5. In the case of single ring resonator, the resonant frequency is determined by the effective inductance and capacitance of its equivalent circuit. The effective inductance is roughly proportional to the enclosed area of SRR, while the effective capacitance depends on the wire width, thickness and separation of the gaps (the gap of the SRR is simplified as a plate capacitor, separated by the gap distance). Nevertheless, after a surface mounted capacitor is inserted into the gap, the effective capacitance of the SRR is decided by the capacitance of the inserted components, because the original capacitance is much smaller compared to the added one. As we stated before, resonance frequency is determined by $1/\sqrt{LC}$. When the capacitance increases, the resonant frequency drops.

By choosing the inserted capacitance, one could easily manipulate the resonance frequency of the ring resonator. For electric resonator, surfaced mounted inductor is also used to increase the effective inductance.

Surface mounted elements have their own disadvantages. The packed surface mounted

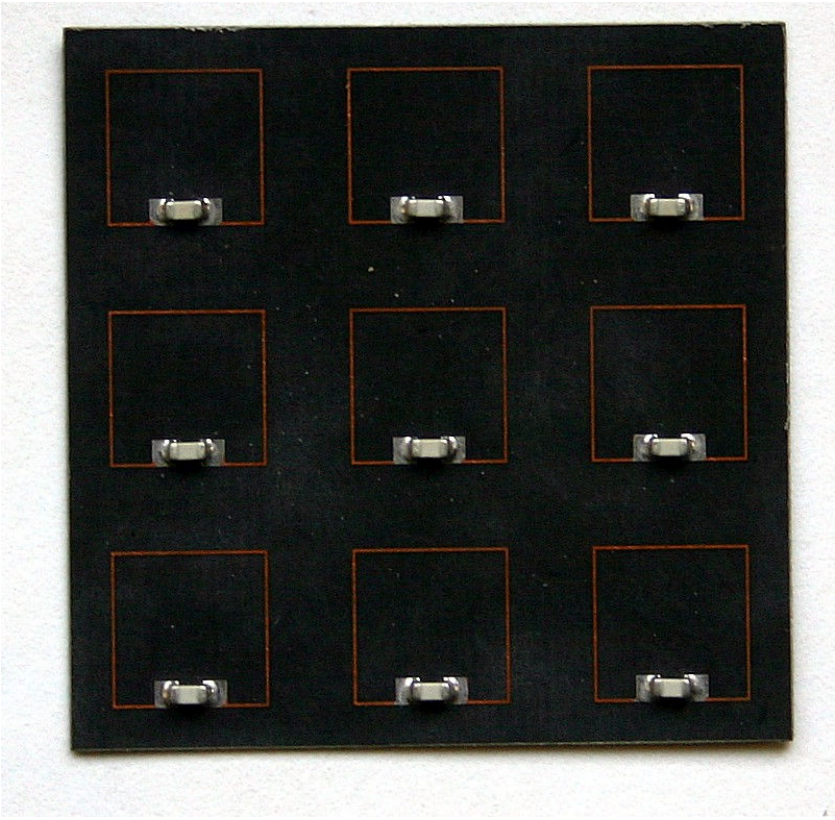

Figure 3.5 Single-ring resonator with surface mounted capacitor soldered in narrow gaps. The sample was provided by Phantom Works of Boeing Company.

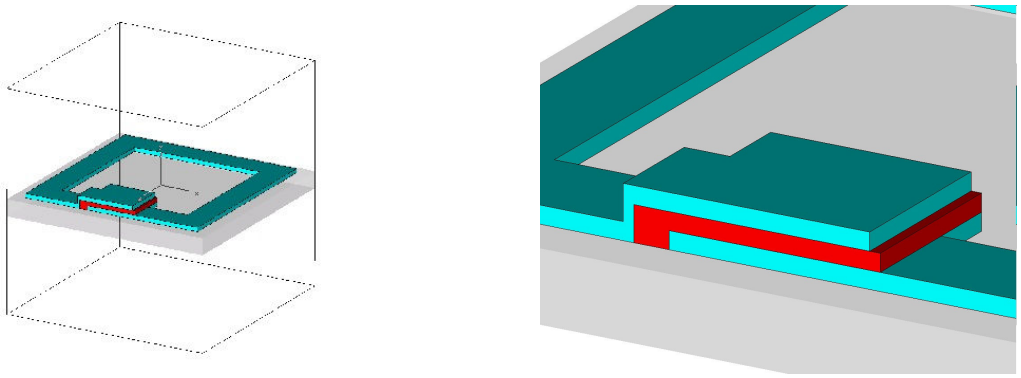

Figure 3.6 Overleaf capacitor SRR and details of the embedded capacitor

RF components available in the market are usually several millimeters and can not be soldered to structures of similar and smaller sizes. To avoid the size limitation, another approach is taken specifically to reduce the ratio (λ/d) of the magnetic component of metamaterial structure: overleaf capacitor SRR.

Overleaf SRR actually forms an embedded capacitor in the ring itself, instead of attaching a discrete component in surface mounted capacitor aided SRR. Fig. 3.6 illustrates the physical structure of such overleaf capacitor SRR.

An example of the fabrication process we used is depicted in Fig. 3.7. Notice that instead of a single layer of metal as in traditional SRRs, there are two layers of metal and one layer of dielectric material. The first layer of metal is deposited on the supporting board, forming the shape of a single ring resonator. Then a thin layer of dielectric material is used to fill in the gap and adjacent part of the wires near the gap. Finally a second layer of metal is deposited on the dielectric layer, with one end connected to the first layer and the other end not.

From Fig. 3.6, it can easily be seen how the two layers of metal and the separating dielectric layer constitute an effective plate capacitor. The capacitance of the embedded plate capacitor can be estimated from the metallic plate area, dielectric constant and thickness of the separating layer. This value could be thousands of times greater than the effective capacitance of the gap in the original single ring resonator, making high λ/d

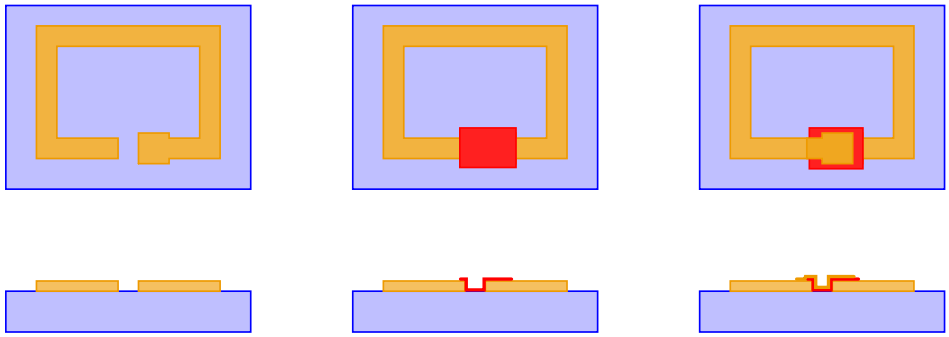

Figure 3.7 Brief overview of the fabrication process of making a overleaf capacitor SRR

magnetic component of metamaterials and their mass production possible. The embedded capacitors do not have the size limitation as a surface mounted RF components do. Furthermore, by choosing the plate size, dielectric constant, and/or the thickness of the dielectric layer, one can easily manipulate the effective capacitance of overleaf capacitor SRR, and hence the resonant frequency.

3.2.1 Numerical Verification of Overleaf Capacitor SRR

We performed simulations using Microwave Studio to verify the effectiveness of overleaf capacitor SRR in lowering the resonant frequency. Here we present a magnetic resonant structure based on the SRR shown in Fig. 3.6. We introduced a very thin layer of SiO_2 via Plasma-Enhanced Chemical vapor deposition (PECVD) to form a plate capacitor, in order to lower the magnetic resonant frequency. In simulation, we designed a overleaf capacitor SRR on top of a 0.2 mm thick square quartz substrate. The quartz substrate has a dielectric constant of 4 and a dissipation factor of 0.0005. The SRR is 2.9 mm long and has a trace width of 0.4 mm. The gap is 0.1 mm and the embedded plate capacitor has a overlapping region of $0.7mm \times 0.8mm$. The unit cell contains one SRR and has the dimension of 3.3 mm in all three dimensions. Plane wave scattering was used to obtain transmission and reflection, with magnetic field oriented on normal direction of the SRR plane.

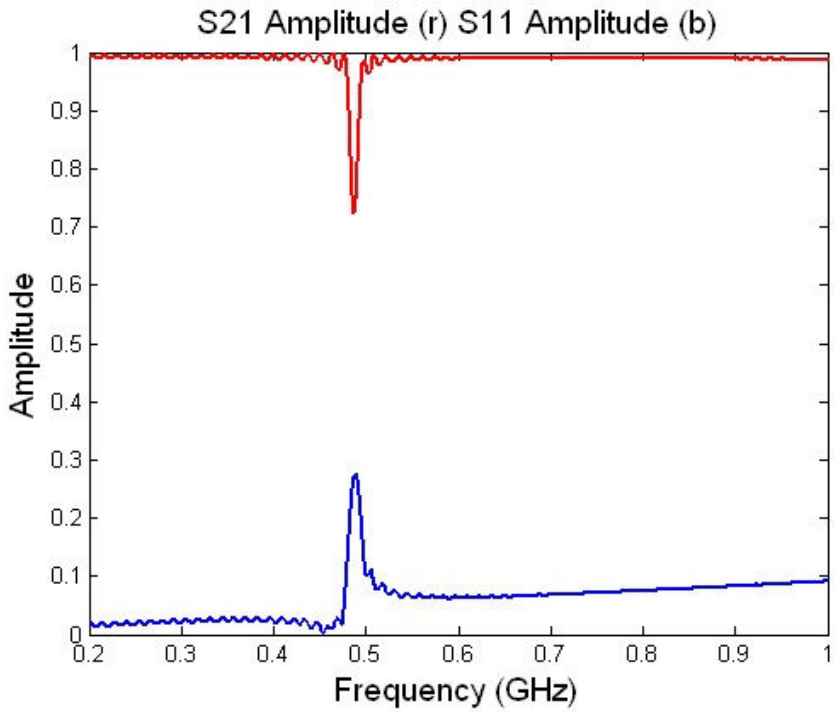

Figure 3.8 Amplitude of transmission (S21) and reflection (S11) versus frequency. The transmission dip indicate where the resonance is.

Microwave Studio simulation results showed that the resonance frequency of the overleaf capacitor SRR is at 0.48GHz, see Fig. 3.8. This translates to $\lambda/d = 190$, which is almost 20 times larger than the λ/d ratio of conventional SRRs.

In Fig. 3.9, we present the results for effective values of the magnetic permeability μ obtained by our retrieval procedure, the same as introduced for the conventional SRR in Chapter 2. A strong resonance of μ can be observed around the frequency of 0.48GHz.

3.2.2 Experimental results of overleaf Capacitor SRR

Experimental efforts were also made to verify the ability to achieve high $\lambda - d$ ratio for overleaf capacitor SRRs. An SRR similar to that in Fig. 3.6 was designed and fabricated in the lab of the Microelectronics Research Center of Iowa State University. Instead of a single-cut one, a 4-cut overleaf capacitor SRR was tested; see Fig. 3.10. The unit cell was 1.5 mm, the SRR was 1.2 mm long, and the wire trace was 0.1 mm wide.

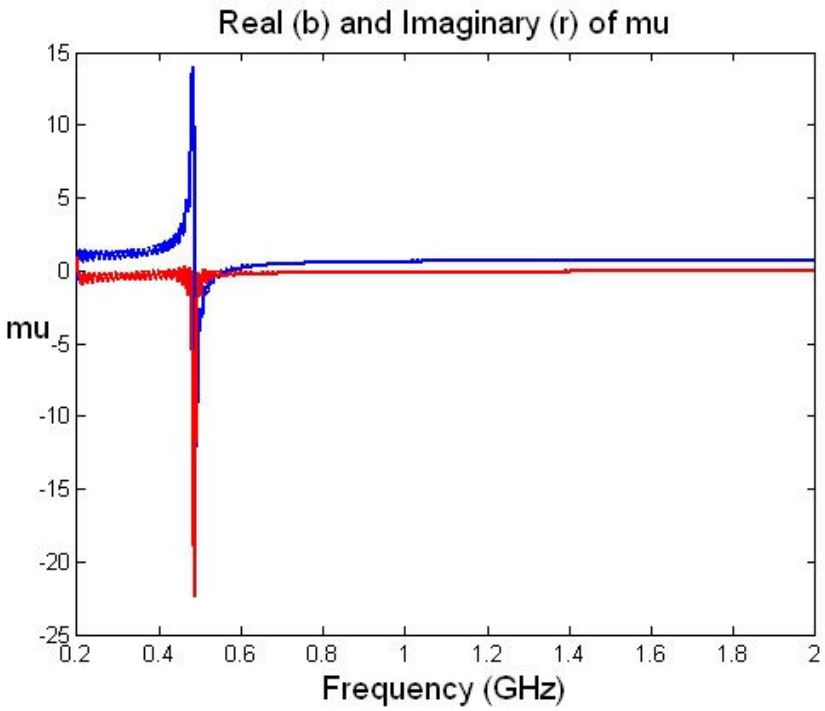

Figure 3.9 Retrieved μ

Microwave Studio simulation results show that the 4-cut overleaf capacitor SRR has a resonant frequency around 5GHz and λ/d ratio is about 40.

To fabricate the SRR, a layer of aluminum ($3.5\mu m$ thick) was deposited on a quartz substrate using the evaporation furnace. After patterning the first layer, a thin layer of polyimide was spinner coated on the ring and patterned. Finally another layer of aluminum is deposited on the polyimide layer and patterned as wanted. A picture of the sample taken through an optical microscope is shown in Fig. 3.11.

Transmission measurements have been performed to test the resonance frequency of the sample. Since a horn antenna operating at 500MHz is very huge and not available in the lab, the experimental setup for measuring transmission through a single substrate of the overleaf SRR structure has been chosen different from measuring transmission through periodic arrays of SRRs in free space by use of waveguide horn antennas. The sample substrate was located between two monopole antennas. Monopole antennas

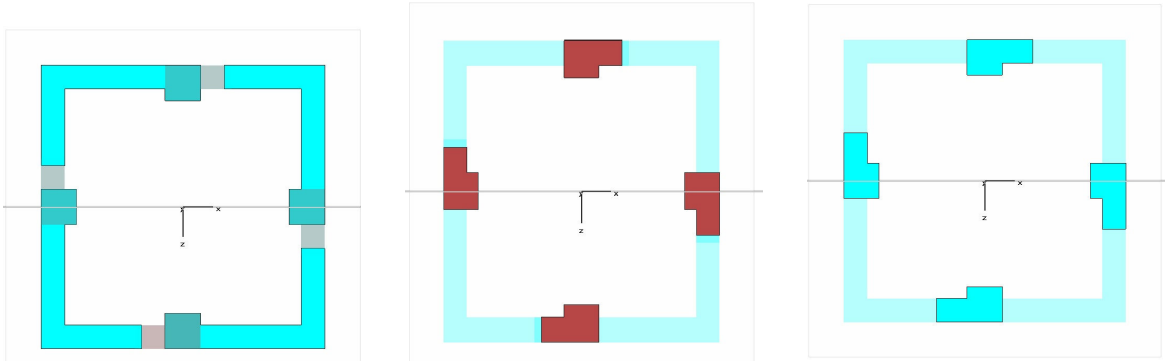

Figure 3.10 Top view of 4-cut overleaf capacitor SRR, from bottom layer to top layer

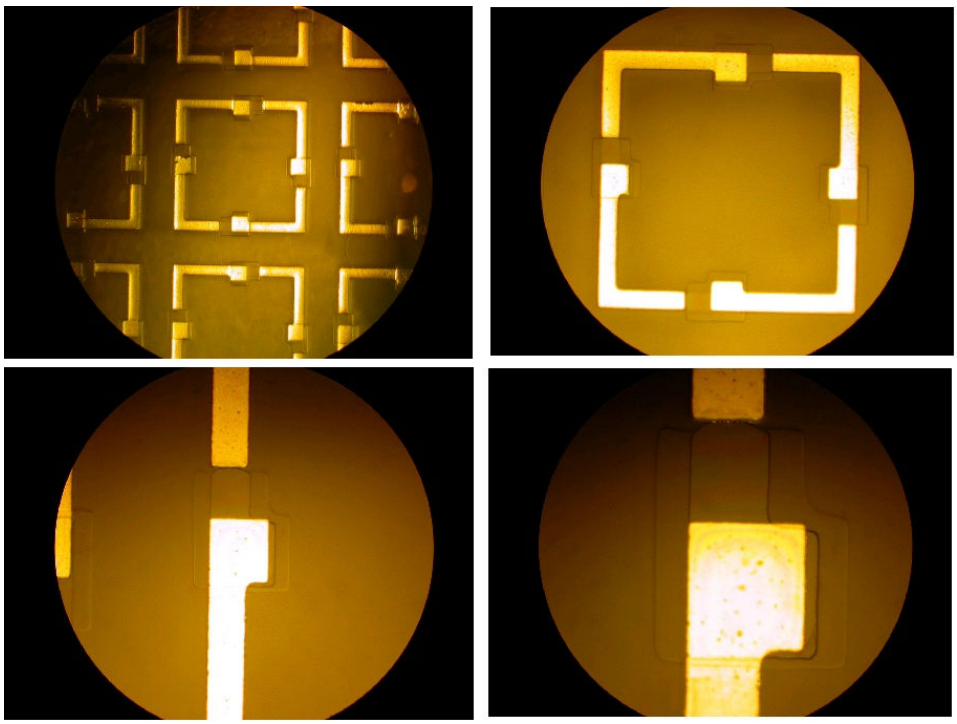

Figure 3.11 The 4-cut overleaf capacitor SRR. Only the first metal layer and the polyimide are shown here.

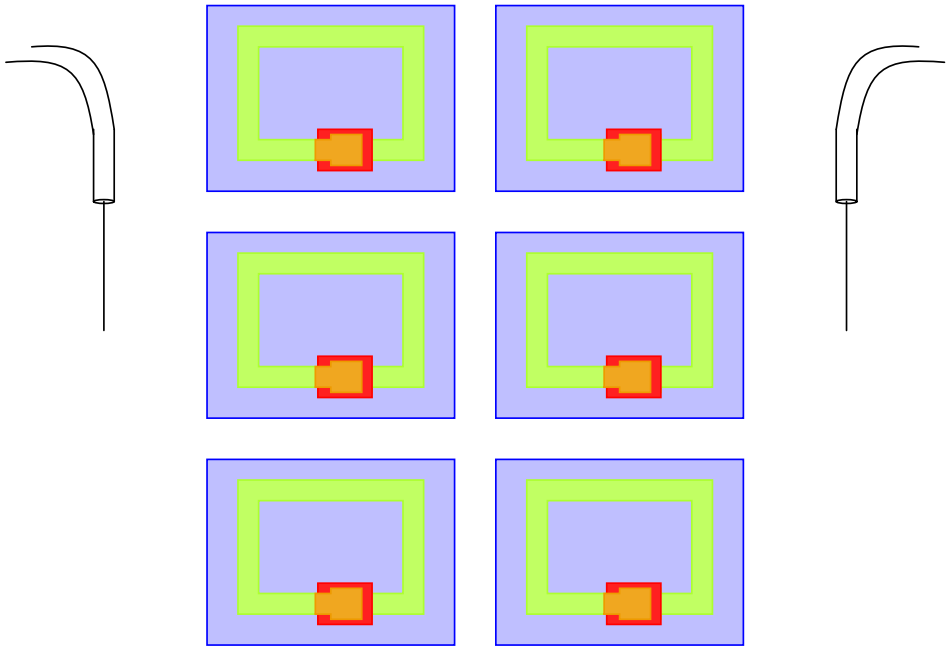

Figure 3.12 Experiment setup for measuring transmission of SRRs through monopole antennas

were used to transmit and detect the EM waves through the single substrate of SRRs. SRRs were placed between the monopole antennas as shown in Fig. 3.12. The monopole antennas were placed very close to the SRR arrays.

Measured transmission spectra are shown in Fig. 3.13. Notice that the measured resonance frequency is 10% higher than the predicted value simulated from Microwave Studio. The reason may be that the real thickness of the polyimide was more than $5\mu m$.

3.2.3 Loss in the Overleaf Capacitor SRR

The overleaf capacitor SRR opens a novel way to manipulate the effective capacitance of the magnetic component of metamaterials. The idea of self embedded capacitor/inductor can be applied to electric components as well. For example, overleaf capacitor can also be added into electric resonator, as shown in Fig. 3.14.

Also the overleaf capacitor SRR has its own limitations. As we noticed in Fig. 3.8, the absorption of the unit cell is not negligible. This is due to the extremely large electric

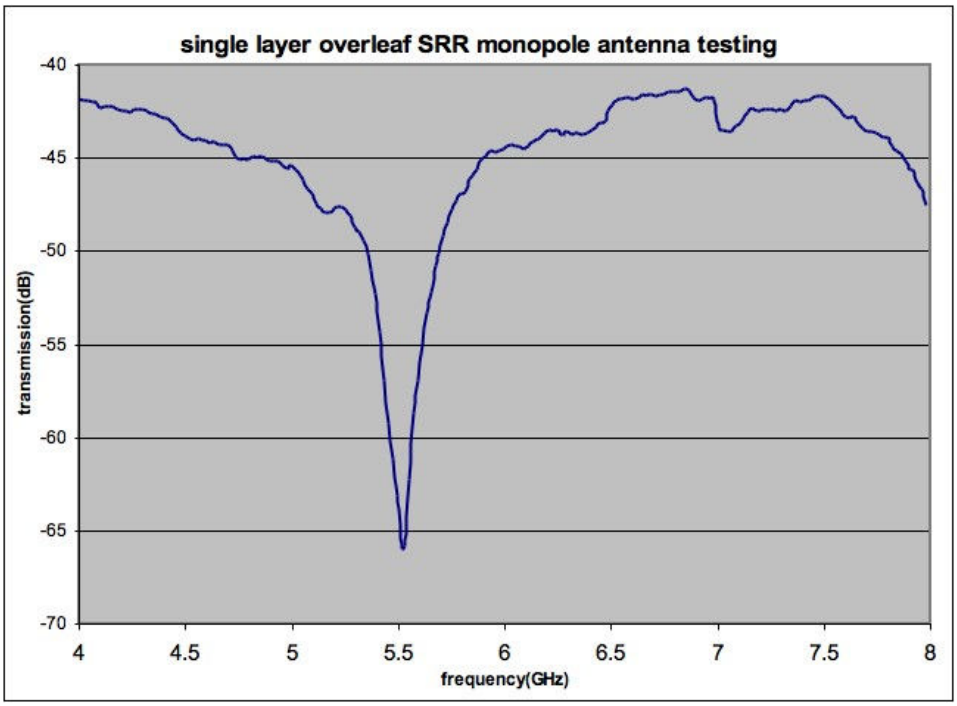

Figure 3.13 Measured transmission of SRRs through monopole antennas

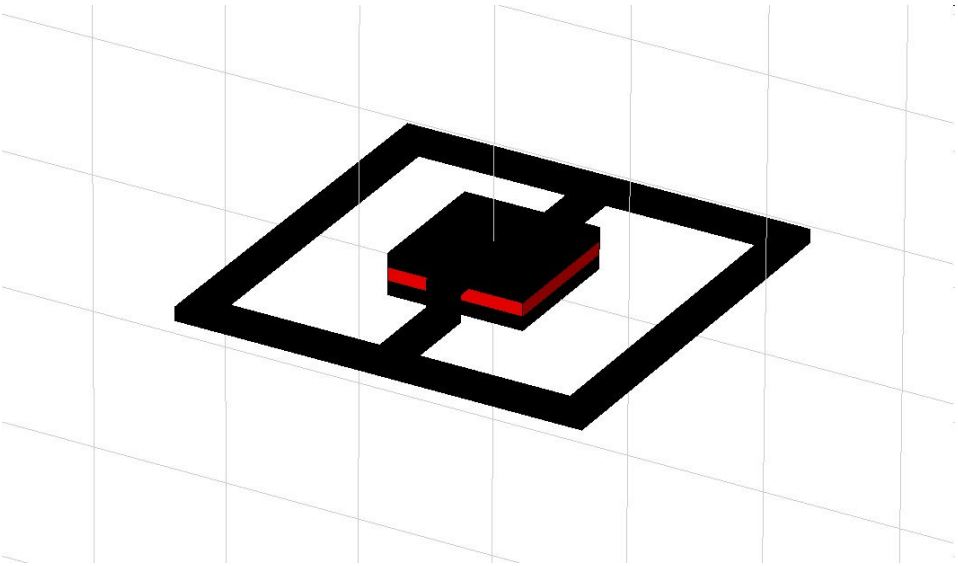

Figure 3.14 Electric resonator with self embedded overleaf capacitor

field concentrated in the embedded capacitor area. The upper and lower metallic plates are only separated by the very thin layer of dielectrics and the magnitude of E field inside could reach several kV/m. Even when the dielectric material has a very small loss tangent, large absorption could occur.

3.3 Comparison of Opposed Rings and Overleaf Capacitor SRR

Although opposed ring was originally designed to remove electric coupling to magnetic resonance due to asymmetry in the geometry of SRR structure, it was found that opposed ring can also be candidate to achieve high λ/d ratio. When the two opposed rings are placed closer and closer, the resonance frequency moves to lower region while other parameter are kept unchanged. When the two rings are only separated by a very thin layer of dielectrics (like several μm), the opposed ring SRR constitute a large plate capacitor. It can be regarded as a evened out overleaf capacitor in the way that instead of constrain the capacitance to a small region of SRR, the pair of rings generate capacitance uniformly.

Compared to overleaf SRR, Opposed-ring SRR has more evenly distributed inner capacitance and is a more symmetric structure.

Comparison has been performed between opposed ring and overleaf SRR of the same unit cell size, wire width, and ring length. Overleaf SRR has a dielectric layer thickness of $0.5\mu m$ and the opposed ring SRR has $1.1\mu m$. Fig. 3.15 shows that they have similar resonance frequencies. For both opposed rings and overleaf SRRs, decreasing the unit cell size in the stacking direction, which is effectively increasing the filling factor, shifts the resonance frequency to lower region. Analytical model has also confirmed this.

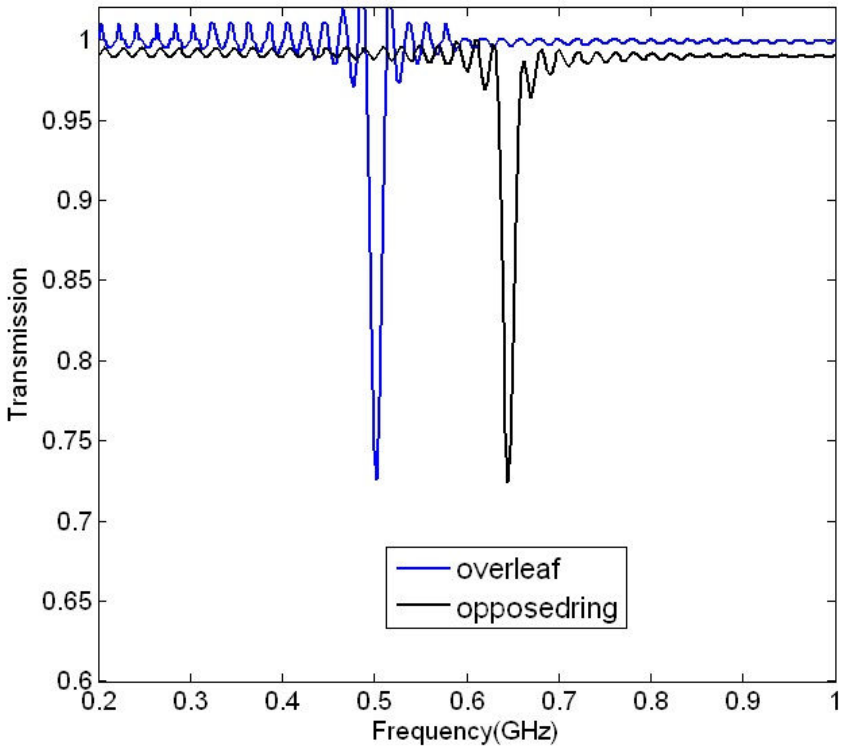

Figure 3.15 Resonance frequency of similar opposed ring and overleaf capacitor SRR

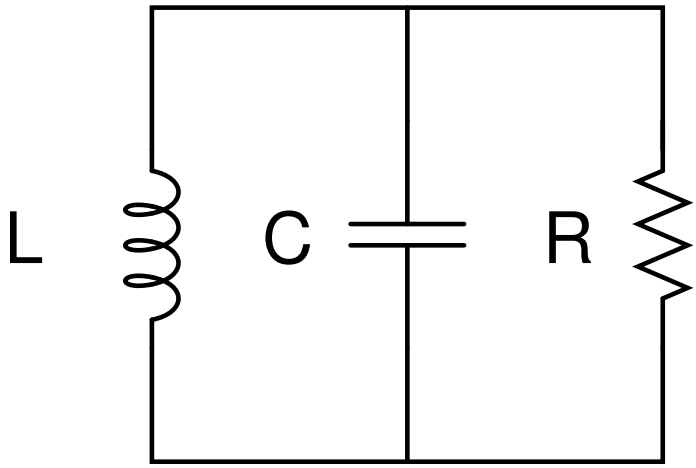

Figure 3.16 Turn-on mode: R has small resistance, the embedded SRR behaves like a closed ring, so no magnetic response shows; Turn-off mode: R works as a huge resistor, the embedded SRR shows magnetic response

3.4 Tunable SRRs

In the previous sections, we discussed approaches to achieve high λ/d ratio symmetric SRRs. However it is also a very interesting project if we can tune the behavior of SRRs and even wires, that is, without change the geometric parameters of metamaterials composed of SRRs and wires, the property (namely refractive index) of metamaterials can be manipulated conveniently.

The approach we employ here is to embed photo-conductive material in the gap of SRRs or cuts between wire structures. By controlling incident light intensity one could affect resistance of embedded material, making the SRR closed or open. When a high-intensity light shines on the SRR, photo-conductive material is in conducting mode and has very small resistance, the embedded SRR is actually a closed ring structure and has no magnetic resonance. When there is no light incident on the photo-conductive material, the material has little conductivity and the SRR works as normal. Fig. 3.16 shows the equivalent circuit.

Simulation test has been taken on a NIM structure operating around 44GHz cf. Fig. 3.17.

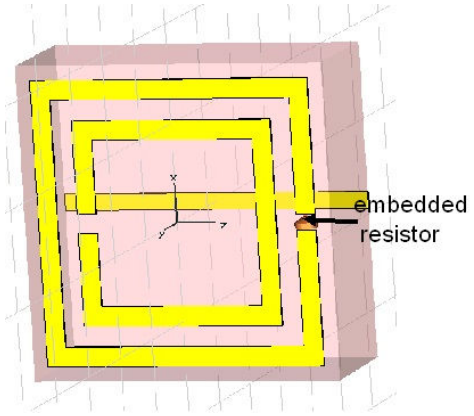

(a)

unit cell = 0.64 mm
SRR size, s = 0.58 mm
SRR linewidth, c = 0.040 mm
Gap between rings, d = 0.042 mm
Inner ring gap, g_i = 0.040 mm
Copper thickness t = 0.003 mm
Rexolite thickness = 0.254mm
Outer ring gap, g_o = 0.033
Wire linewidth, w = 0.034

(b)

Figure 3.17 Plot of photoelectric material embedded NIM structure and the parameters

Photoelectric material is inserted in the gap of the outer ring of the SRR.

When the resistance of the inserted photoelectric material changes from 10M ohm to 1K ohm, the refractive index of the NIM unit cell increases from -1.6 to near zero. It proves that controlling the intensity of incident light can be an effective way to manipulate the electromagnetic property of the photoelectric material embedded NIM structure.

3.5 Summary

To obtaining high λ/d ratio metamaterial structure, the design of overleaf capacitor and opposed ring SRR were proposed. Theoretical, numerical, and experimental results indicated that they both work. Ratios of up to $\lambda/d \approx 200$ have been practically achieved. Opposed ring SRR has more evenly distributed inner capacitance, and is a more symmetric structure compared to overleaf SRRs. An effective and convenient way to tune the behavior of SRRs is also presented.

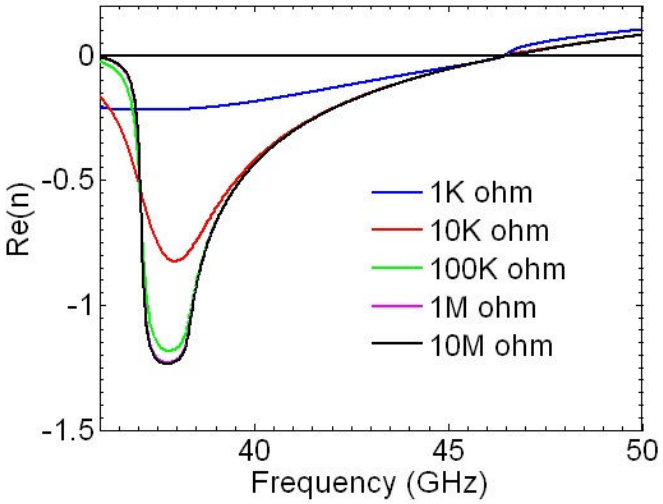

Figure 3.18 Refractive index plot for different resistance

CHAPTER 4 Negative refraction in Photonic Crystal

Left-handed-materials are materials with simultaneously negative dielectric permittivity ϵ and negative magnetic permeability μ. The phase velocity of the light wave propagating inside this medium is pointed in the opposite direction of the energy flow. Thus, the Poynting vector and wave vector are anti-parallel, consequently, the light is refracted negatively. Several theoretical and experimental groups have investigated negative refraction behavior of left-handed materials.

For LHM based on photonic crystals, Notomi studied light propagation in a strongly modulated two-dimensional PC [16]. Luo et al. have studied subwavelength imagining in PCs [23]. Cubukcu et al. demonstrated experimentally single beam negative refraction and superlensing in the valence band of 2D PCs operating in the microwave regime [5]. Foteinopoulou et al. emphasized the time evolution of an EM wave as it hits the interface between a right-handed and a LH material interface [7]. Pendry suggested that a slab of lossless LHM with both ϵ and μ equal to -1 should behave as a perfect lens [33], i.e, the details smaller than wavelength as well as the larger ones could be reproduced by such a lens. The reconstruction of the evanescent wave components is the key to such perfect focusing. It is shown how the evanescent waves get amplified upon reaching the interface between a RH and LH medium and consequently how they participate in improving the quality of the image. Homogeneous metamaterials and PCs were used to demonstrate the effect. The main challenge is to find a structure with n=-1 for which the matching condition are verified with no reflections. The candidate structure should have three characteristics. First, it should exhibit almost isotropic equal frequency surfaces (EFS)

in a band region with $v_g \cdot k < 0$, with k being the wave vector in the first Brillouin zone (BZ) and v_g is the group velocity. The latter implies $S \cdot k < 0$, where S is the time averaged quantity of the spatial average of the Poynting vector within the unit cell, and thus LH behavior. Second, it should guarantee the absence of any higher order Bragg reflections for any angle of incidence. Finally it should guarantee single beam propagation.

4.1 Negative Refraction and superlensing in 2D rectangular PC

In this section we propose an almost ideal structure based on a PC. The proposed structure meets all the required conditions stated above and has a high transmission at the desired frequency as well as a refractive index very close to n=-1. As it will be discussed below, the refractive index ranges from -0.97 to -1.22 because of the anisotropy. Additionally, with an appropriate cut and a specific termination of the surface, the proposed structure focuses the image in a better way by exciting the surface waves and enabling them to contribute toward the quality of the image. Furthermore, for different incident angles, the cut structure demonstrates a high transmission as well as a maximum coupling with the surface modes at the interfaces.

4.1.1 Structure of the 2D rectangular PC

The proposed structure consists of a triangular array of dielectric bars with a dielectric constant $\epsilon = 9.61$ in air. The dimensions of each bar in the x and y directions are, respectively, $r_x = 0.40a$ and $r_y = 0.80a$, where a=1.5875 cm is the center to center separation between bars. The length of each bar is l=45.72 cm. Fig. 4.1 shows the structure with more details. Only the TM modes are considered here (the E field is parallel to the rods).

The plane wave method was used to compute the photonic band structure as well as the EFS, which was performed by S. Foteinopoulou. Some of the theoretical results were obtained using the finite difference time domain (FDTD) method by R. Moussa. This method shows a time and space evolution of the emitted EM waves. More details of this algorithm can be found in Ref. [47]. In all the FDTD simulations we report, LIAO boundary conditions [21] are used.

Depending on the desired conditions for the case under study, the source emits a monochromatic TM polarization of desired dimensionless frequency. A Gaussian source (Gaussian in space and almost monochromatic) is placed outside the structure to check the negative refraction. However, a point source also excites the surface waves at the interface between RH and LH material. The photonic band structure as well as the EFS in k space are shown in Fig. 4.2. The quantity (fa/c) is the dimensionless frequency where c is the velocity of light and a is the lattice constant. A region in the second band, extending from 0.313 to 0.41, has $v_g \cdot k < 0$ and is of particular interest. To study the system and to compute the refractive index, the EFS are plotted for different frequencies. Note that the EFS consist of the allowed propagation modes for a specific frequency and in our case, they have closed concave like form. Within the second band the shape of the EFS tends to became circular for higher frequencies and reproduces the symmetry of the system for lower frequencies. It is important to notice that in contrary with the triangular lattice with circular rods for which the hexagonal symmetry is conserved on the lattice as well as on the scatterers, this structure with rectangular rods loses its hexagonal symmetry for the scatterers when the wave is traveling along a specific direction. Thus the breaking of the symmetry gives some anisotropy in the structure. Thus, the EFS are not totally isotropic because of the breaking of the symmetry. Therefore, the computed phase refractive index of our structure using the EFS plot is somehow affected by the anisotropy. It is not exactly equal to -1. In fact, for different incident angles it ranges from -0.97 to -1.22.

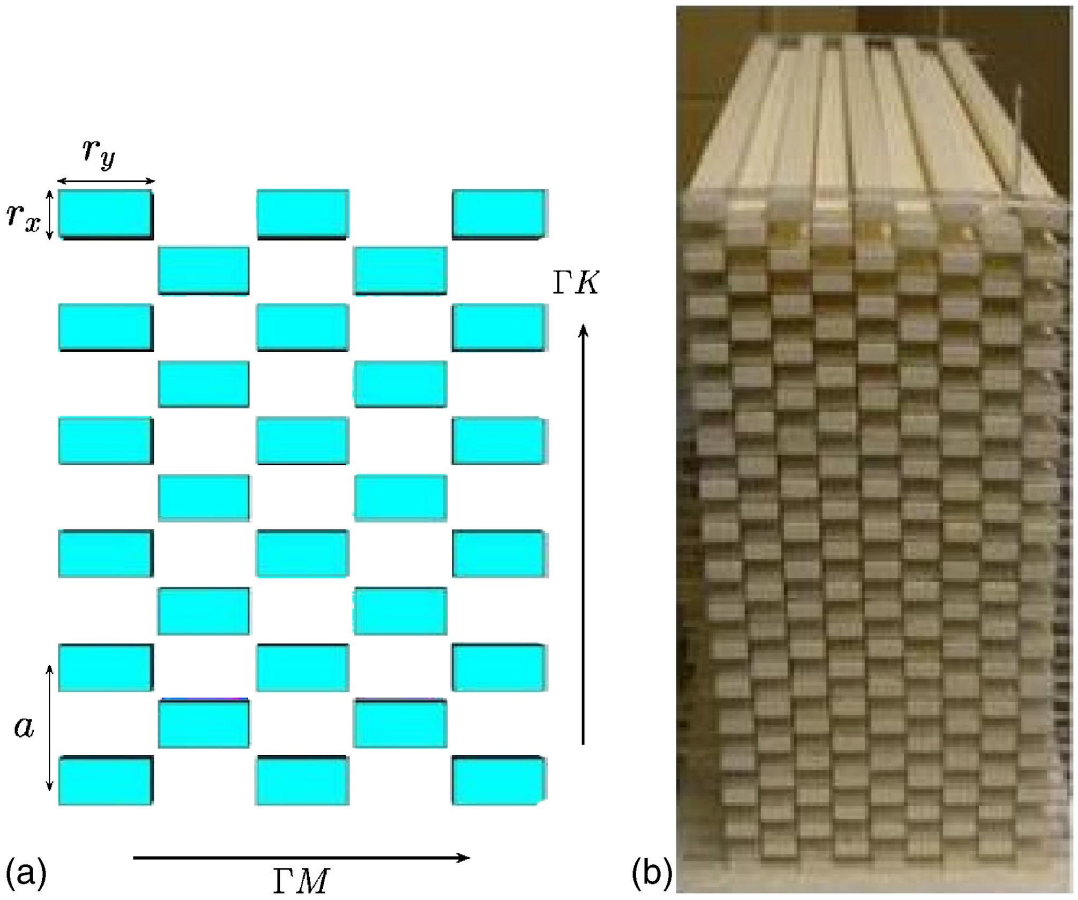

Figure 4.1 (a) A triangular array of dielectric bars in air with rx = 0.40a and ry = 0.80a, where a = 1.5875 cm is the lattice constant. (b) A picture of the structure with 33 layers in the lateral direction and nine layers in the propagation direction.

4.1.2 Theoretical prediction and Experimental measurements of Negative Refraction

Transmission measurements are performed to verify and test the negative refraction and superlensing. The experimental setup consists of an HP 8510C network analyzer, a waveguide horn antenna as the transmitter, and a monopole antenna as the receiver. The PC used for the negative refraction experiment has nine layers in the propagation direction ΓM and 33 layers in the lateral direction ΓK . The interfaces are along the ΓK direction. In all the experimental and theoretical results, the electric field is kept parallel to the bars. The operational frequency that leads to a structure of approximately n = -1 is 6.5 GHz which correspond to a dimensionless frequency of fa / c = 0.345. For the negative refraction the horn antenna is oriented such that it makes an angle with the normal to the ΓK interface.

To examine the negative refraction, we first measure the transmission along the first interface along the ΓK direction without the PC. We repeat the measurement but this time with the PC and calculate the transmission in the vicinity of the second interface. The results are plotted in Fig. 4.3. It is shown clearly how the center of the outgoing Gaussian beam is shifted toward the left-handed side of the center of the incident beam. This is a clear indication of the negative refraction occurring inside the structure. To get a further insight about the negative or positive shift, Fig. 4.4 explains in detail in which cases we have positive or negative refraction.

It is important to notice that experimentally we did observe the negative refraction for different angles. This confirms that the negative refraction is coming from the almost circular EFS, when $v_g \cdot k < 0$. For a particular angle of $\theta = 30(deg)$, the lateral shift was 3.2 cm which correspond to a negative angle inside the LH PC of -15 (deg). We also have done experiments for different incident angles, and always found negative refraction. In particular for incident angles of 45 and 60 deg , the refracted angles are -20 and -30 (deg) , respectively.

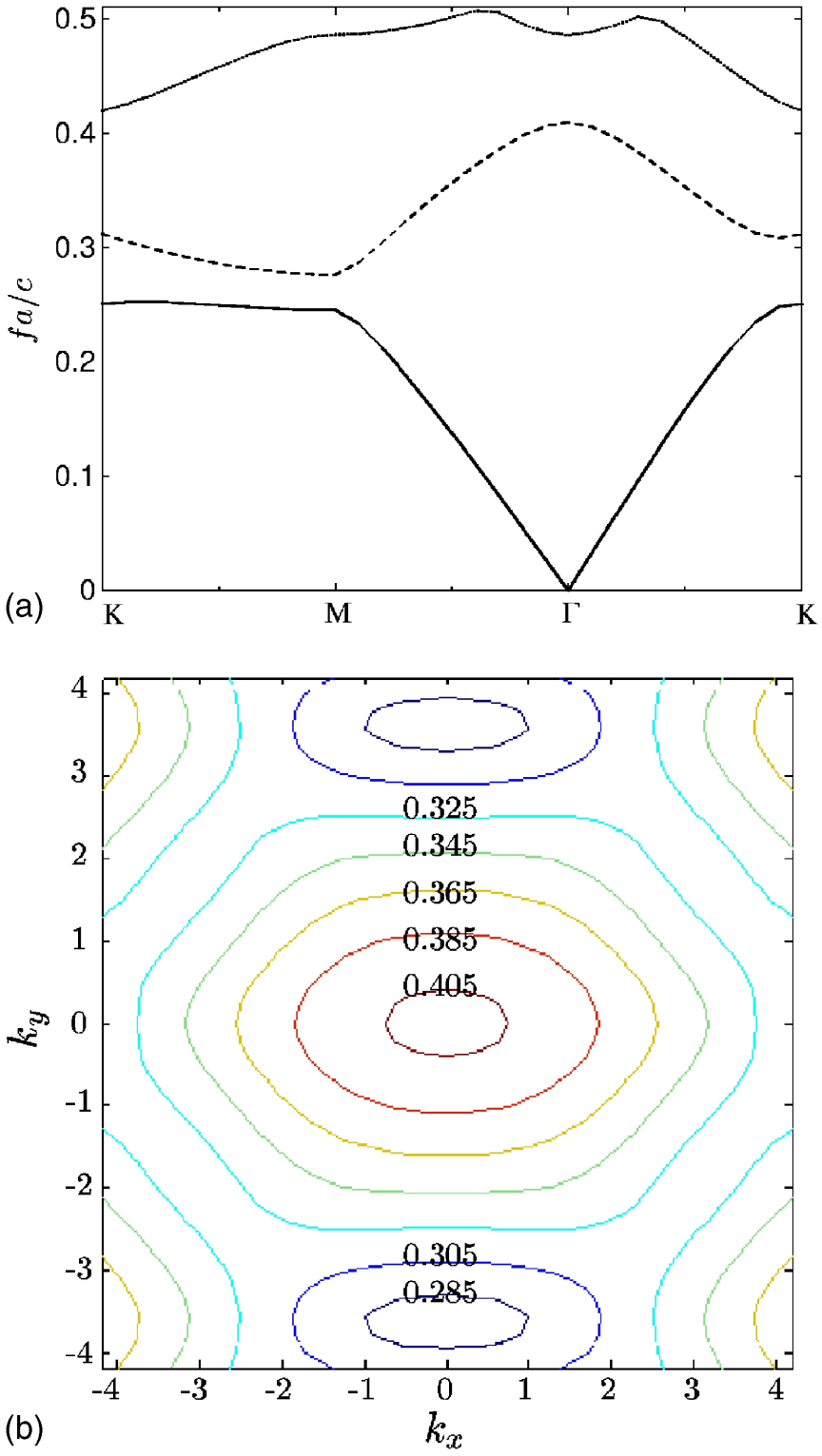

Figure 4.2 (a) The photonic band structure for the ΓM polarization. (b) The EFS with different dimensionless frequencies shown on the corresponding curves.

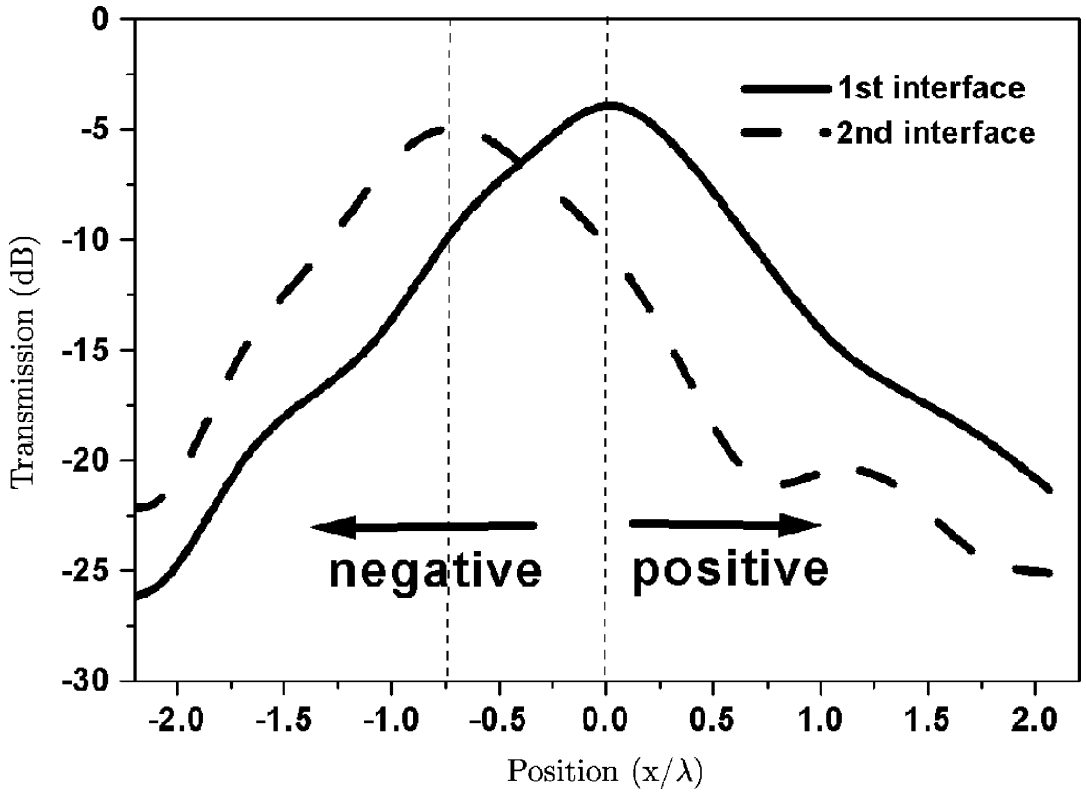

Figure 4.3 The transmission at the first (solid line) and second interface dashed line of the PC vs the lateral position. Arrows indicate the refracted beam's direction depending on positive or negative shift.

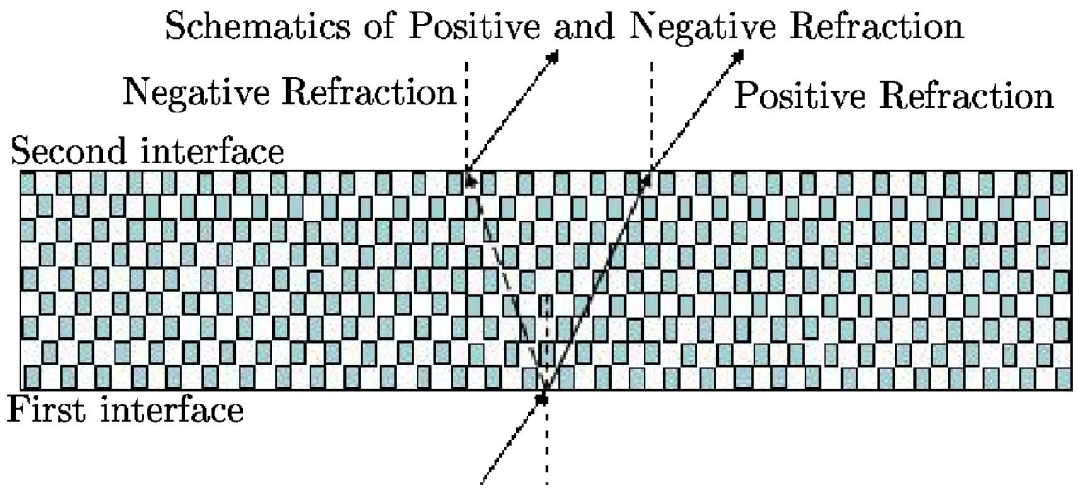

Figure 4.4 Schematics of positive and negative refraction. For negative refracted beam, the center is shifted to the left-hand side of the incident beam and for the positive refracted beam, the center is shifted to the right-hand side of the incident beam.

Further insight about the field distribution inside this structure can be gained by observing the E field inside a LH PCs slab plotted in Fig. 4.5 after 77.33T, where $T = 2\pi/\omega$ is the period of the incident waves. The structure length along the lateral direction is about 13.8 and about 2.98 in the propagation direction. A Gaussian beam source with = 46 mm is placed outside the PC making an angle = 30 (deg) with respect to the interface which lies in the ΓK direction. The FDTD simulation is performed by discretizing the real space into a fine rectangular grid of a / 54 and a / 92 for the x and y axes, respectively . A time step of $\delta t = 24.90ps$ is used. The distribution of the field inside the PC shows how the beam is negatively refracted inside the PC and refracted in parallel way to the incident beam outside the PC. The theoretical result is in a good agreement with the experiment since it gives a negative refracted angle of about -15 deg. Theoretical agreement also exists for the other incident angles.

An important advantage of this structure is its property to allow single beam propagation. The structure was designed in such a manner that only one beam propagation is allowed eliminating the undesired Bragg waves inside the PC. One of the interesting

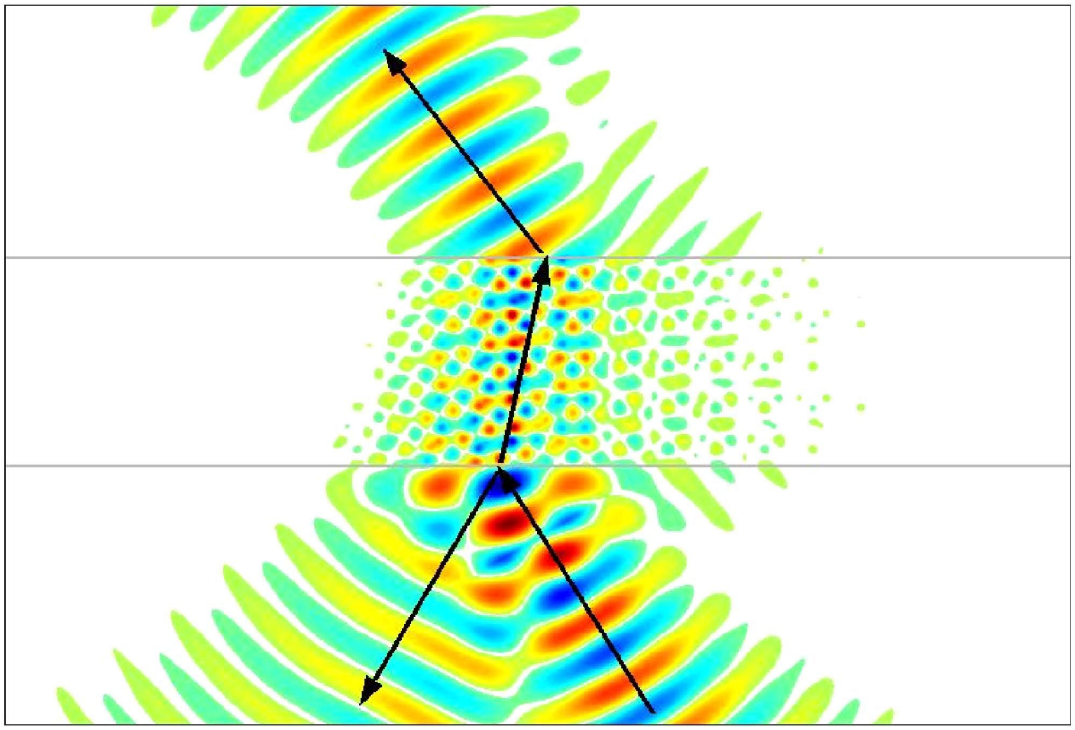

Figure 4.5 The E field of a Gaussian beam propagating along 30 deg direction after 77.33T. The structure is 13.8 λ in the lateral direction and 2.98λ in the propagation direction.

features of this structure compared to the other LHM based on proposed PCs is its high transmission. Fig. 4.6 displays the transmission versus the dimensionless frequency. The experimental curve shows the high transmission of the structure over a wide range of frequencies including the operational one. The arrows in this figure show the theoretical indication of the gaps. As predicted by the band structure, the experimental curve shows two gaps in the ΓM direction one between 0.25 and 0.276 and the other one starting at 0.41. Thus, the agreement between the band structure and the experimental curve is very good.

In order to get an idea about what is happening inside the structure we examine the transmission in both directions. Fig. 4.7 shows the transmission in the ΓM and ΓK direction versus the frequency. This structure at the dimensionless operational frequency 0.345 has a good transmission in the ΓM direction and a weak transmission in the ΓK direction. A weak transmission in the ΓK direction enhance the transmission in the propagation direction which will be a critical issue for the superlensing phenomenon. It was argued that the focusing seen at the edge of the first band in a square lattice was not due to negative refraction but to anisotropic propagation resulting to the funneling effect. This is not the case in our structure. As we will show later, the focusing and the superlensing in our structure relies on negative refraction and on coupling to the surface states.

4.1.3 Superlensing phenomenon

In order to investigate the superlensing phenomenon, we experimentally measure the intensity of the focus for the same structure used in the transmission measurements 33 layers in the lateral direction and 9 layers in the propagation direction. Two probes are used. The first one is placed at a distance of 0.2λ from the first interface of the PC and the second one at the same distance from the second interface. We measure the transmission with and without the PC. Fig. 4.8 shows the two resulting curves.

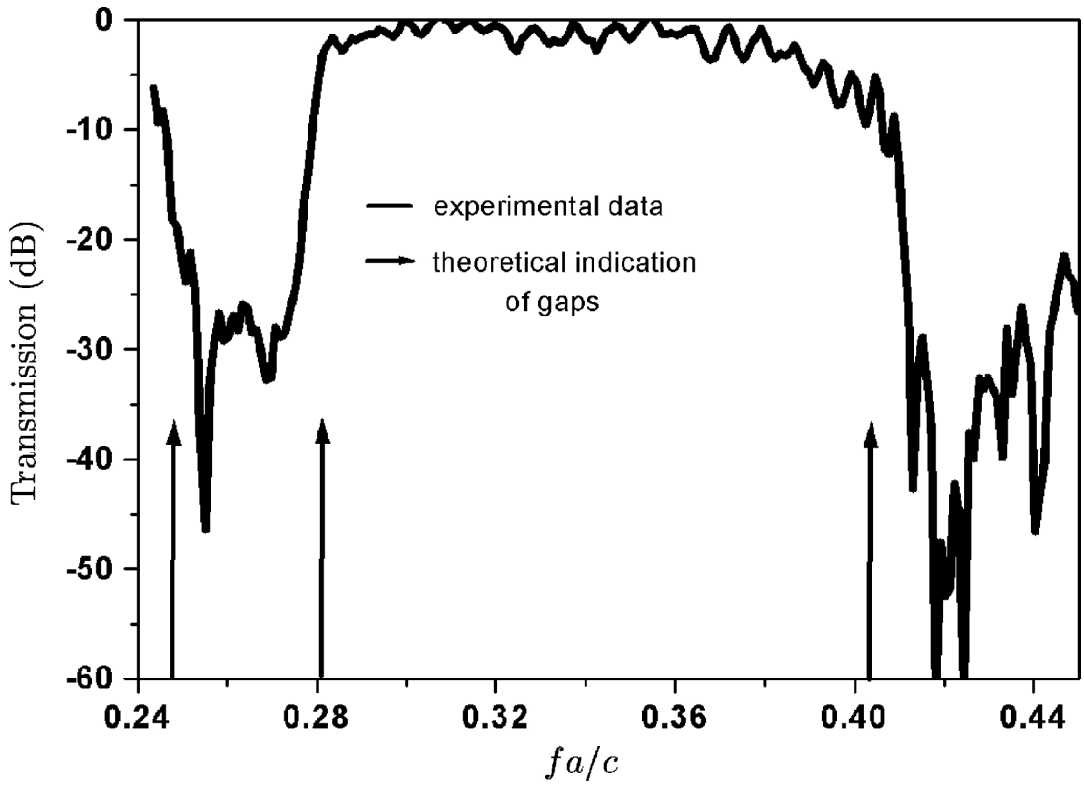

Figure 4.6 The transmission along the M direction vs the dimensionless frequency. The solid arrows indicate the theoretical gaps as calculated from the band structure.

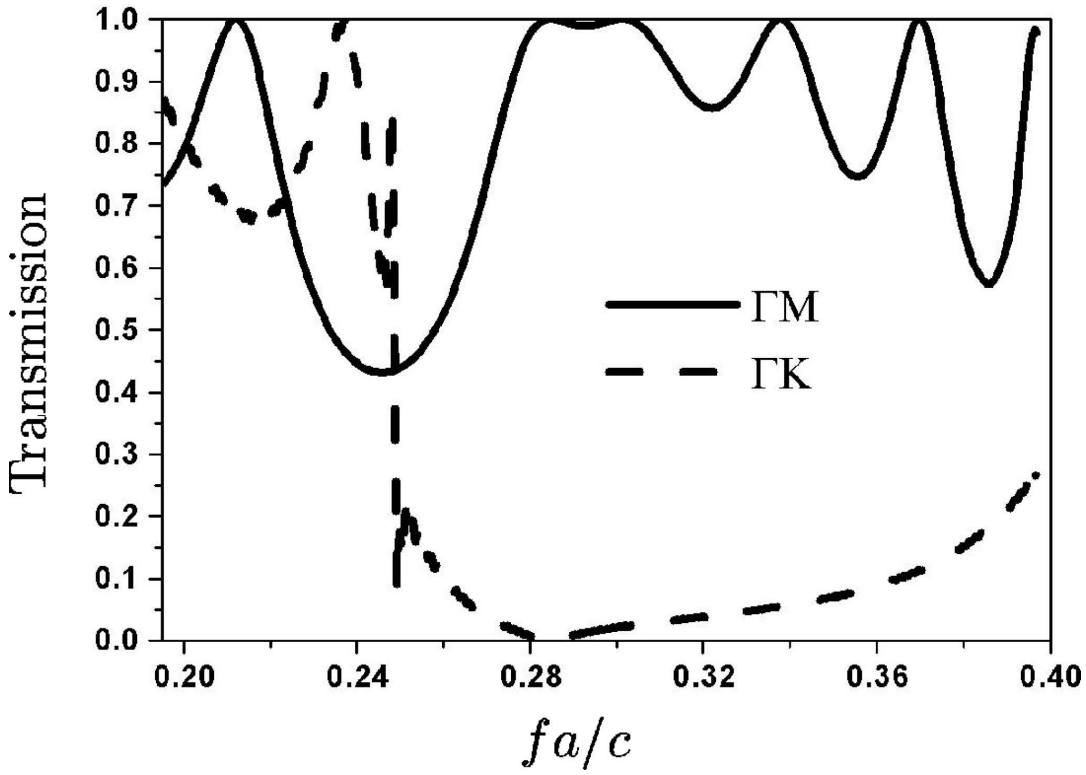

Figure 4.7 The transmission vs the frequency for both the ΓM and ΓK direction.

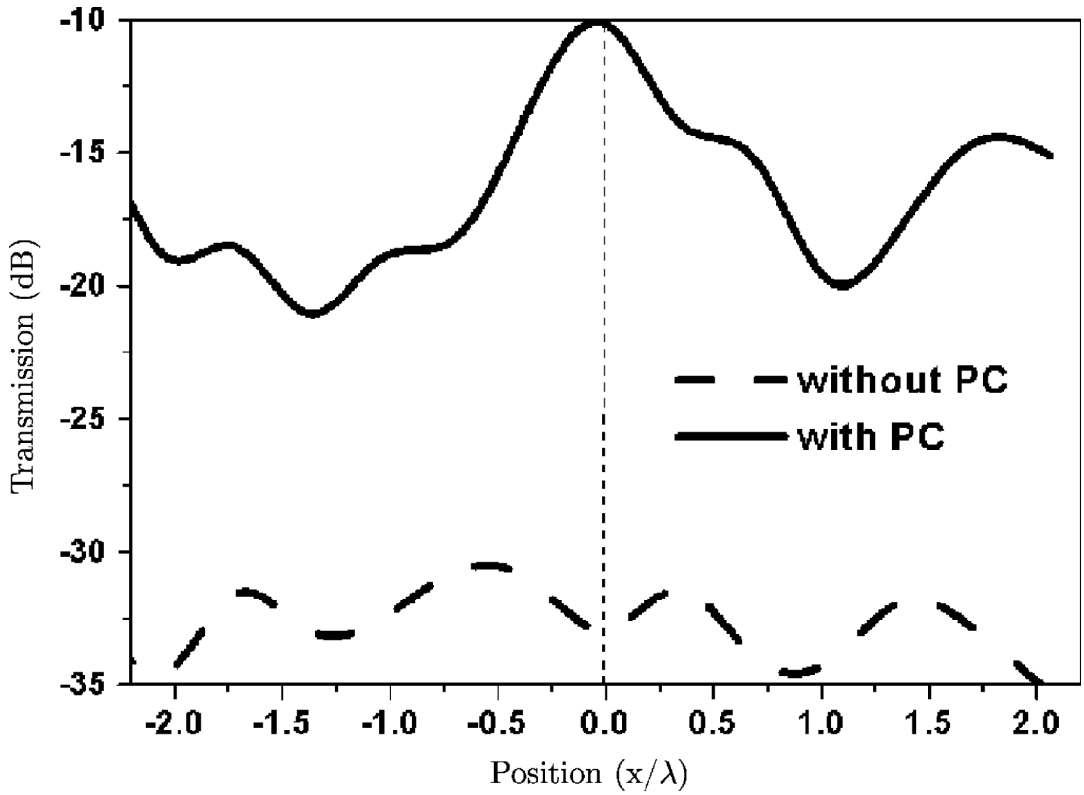

Figure 4.8 The transmission vs the lateral position of a probe placed at a distance 0.2λ from the first interface without the PC dashed curve and with the PC solid curve at 6.5 GHz or a dimensionless frequency $fa/c = 0.345$.

This figure demonstrates the high intensity of the focus and that the transmission is enhanced by more than 20 dB for the setup with the PC compared to the one without the PC. The solid curve also shows a high transmission at the edge of the structure at $x/\lambda \cong 1.75$. This might be due to the limited lateral length of the structure and to the support station which might give some reflection at the edge.

Theoretically, we investigate the superlensing within a slab of PC with a dimension of 20.7λ in the lateral direction and 1.20λ in the propagation direction. A point source with a dimensionless frequency 0.345 placed at a distance 0.15λ from the first interface of the PC is used. A time step of $\delta t = 26.5ps$ and a fine rectangular discretization mesh of $a/40$ and $a/92$ in the x and y direction are used. Fig. 4.9 (a) and Fig. 4.9 (b) show

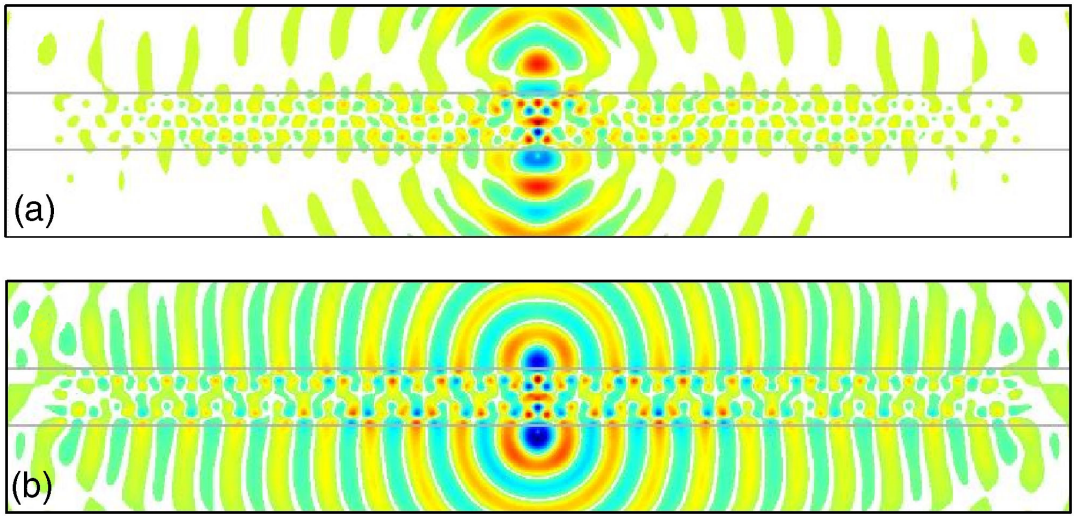

Figure 4.9 Snapshots of the E field after 68.49T of a point source located at 0.15 and its image through a PC slab of 20.7λ in the lateral direction and 1.20λ in the propagation direction. a shows the complete structure and b shows the structure with a surface cut of 0.10a.

the snapshots of the E field after 68.49T for the complete structure and the one with 0.10a termination. By the termination or cut 0.10a we mean that we cut 0.10a from the first and last rows of the bars. Notice that in order to excite the surface waves at the interface, we studied different terminations of the surface. Among the different cuts, one surface termination succeeds in exciting the surface waves as shown in Fig. 4.9 (b) . In this case the cut was about 0.10a. For both Fig. 4.9 (a) and Fig. 4.9 (b) a focus is obtained. However, a better image with a higher intensity is obtained when surface waves are involved. The surface waves in Fig. 4.9 (b) are clearly shown as propagating along both the ΓK interfaces. As shown in Fig. 4.9 (b), the image is almost at the same distance as the source. We did check other distances of the source from the first interface. Indeed, a distance of 0.30 λ was examined. As expected the image moves closer to the second interface at roughly 0.09 . However, the distance of the image from the second interface is not at the same position as if our structure was isotropic with a refractive index equal exactly to -1. This is due to the anisotropy of our structure.

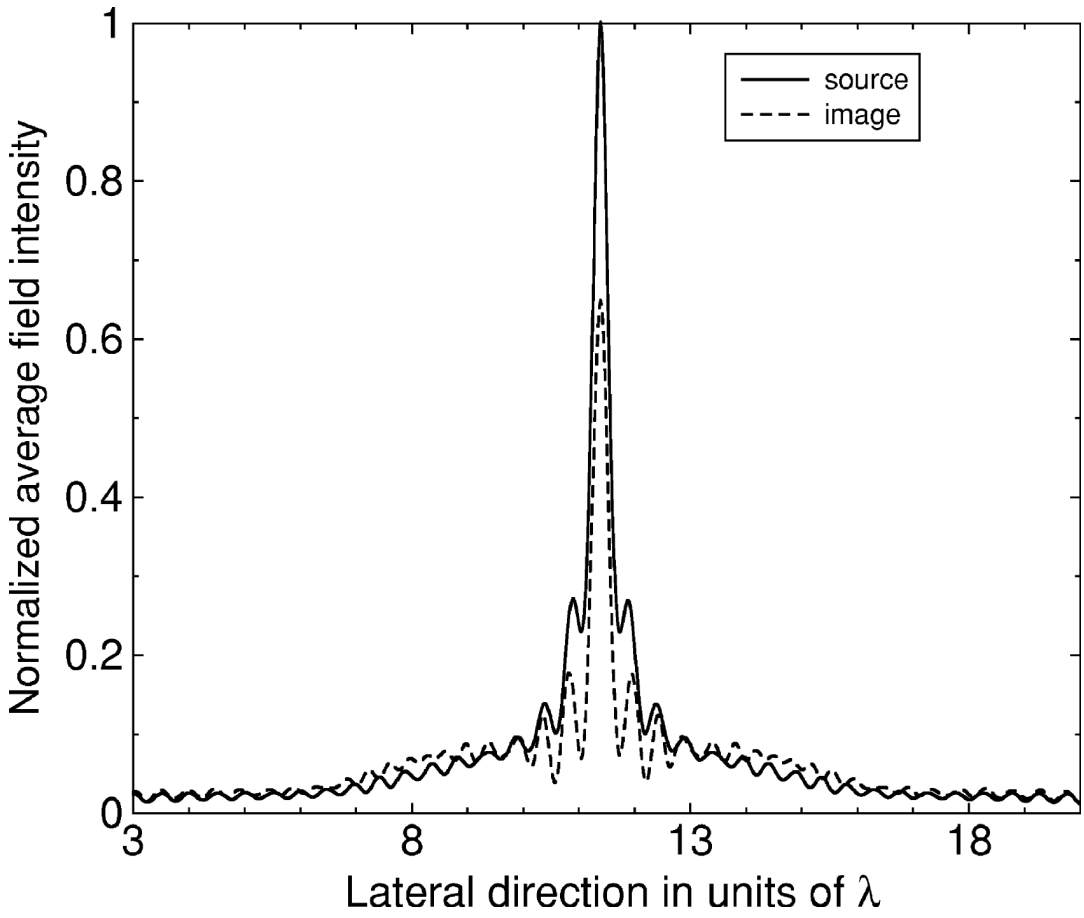

Figure 4.10 The normalized average eld intensity at the source black curve and image plane dashed curve vs the lateral direction.

One way to verify the good quality of the image compared to the source is to plot the average field intensity over a period at both the source and image planes. Fig. 4.10 displays the normalized average field intensity versus the lateral direction for the cut structure. The full width at half maximum (FWHM) of the image beam is 0.35 λ and it is almost the same as the FWHM at the source. This result shows that the cut structure, which supports surface waves focuses in perfect way the object. Thus with a source that is not too close to the structure 0.15 λ we succeed in exciting the evanescent waves and achieving a better focus.

Apparently our structure with 0.10a cut surface seems to be a good candidate for superlensing because we achieved a quite high transmission over a wide range of angles.

Fig. 4.11 presents the transmission versus the angle of incidence for different values of surface terminations. By trying different terminations we managed to optimize the transmission. For the complete structure, the transmission start at 80% for normal incidence, it gets high for a short range of angles then it drops to less than 20% for angles larger than 70 deg . However, the structure with a surface termination of 0.10a see Fig. 4.11 shows the maximum transmission for all incident angles. Thus, the transmission is about 95% for angles up to 40 deg , and more than 80% for angles up to 65 deg and more than 50% for angles up to 78 deg . This result shows first how the transmission gets enhanced by the means of the excitation of the surface waves for a nonhomogeneous structure. Second, high transmission over a wide range of incident angles excludes the possibility of the funneling effect, and accentuate the fact that the negative refraction in our structure is purely a result of LH behavior5 and not a preferred propagation direction.

4.1.4 Conclusion

In conclusion, we have systematically studied a LH structure based on a rectangular PC with a negative refractive index. Our experimental and theoretical results show the negative refraction as well as the superlensing phenomenon in this structure. Furthermore, surface waves at the interface between air and the PC are excited within a specific termination of the surface allowing the reconstruction of the evanescent waves for better focus. The calculated average field intensity in the source plane as well as in the image plane shows almost the same full width at half maximum demonstrating the perfect image reproduced by this structure. Its high transmission along a wide range of angles makes it a good candidate for observing LH behavior in PCs.

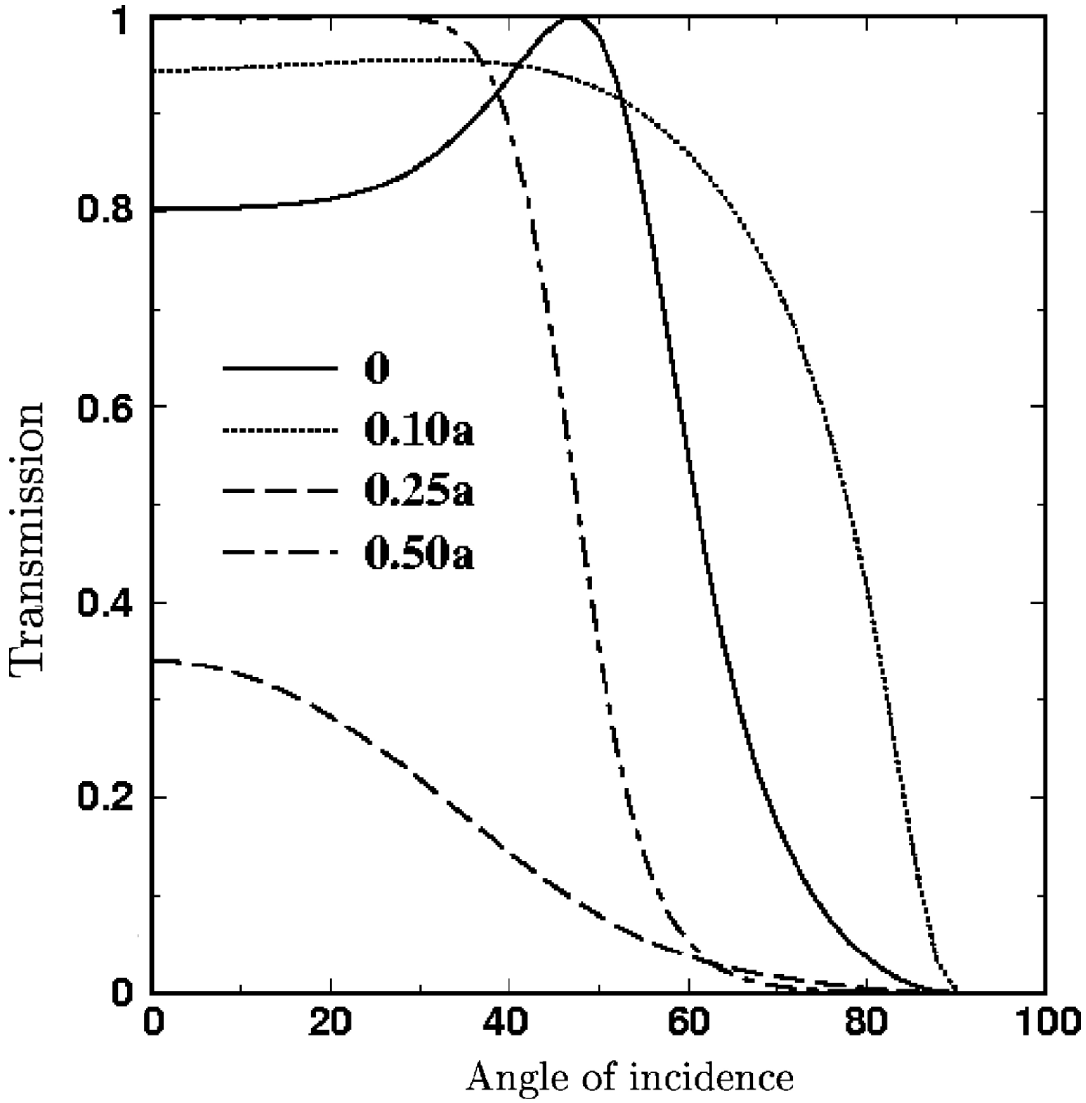

Figure 4.11 Transmission vs the angle of incidence for different surface terminations.

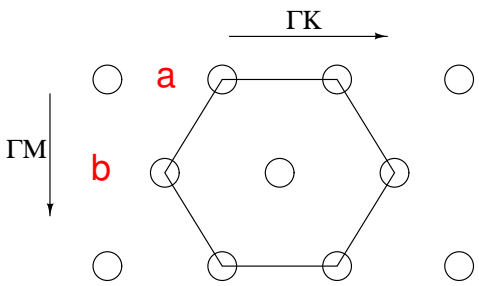

Figure 4.12 Real Space Lattice

4.2 Negative refraction in 2D Wedge PC

Due to the unique properties of the PCs, only a wedge type of experiment can unambiguously determine the rightness of the PC and determine the sign of $\mathbf{S} \cdot \mathbf{k}$, ($\mathbf{k}$ is the wave vector in the first Brillouin zone (BZ) and $\mathbf{S}$ is the pointing vector). Such wedge type of experiment was proposed earlier [8]. However, no experience has been reported that can unambiguously determine the rightness of the PC. This section presents the results of such experimental realization. Two major difficulties are encountered. First, how should the wedge be designed in order to avoid ambiguities and complications in interpreting the results [9]. Second, it is well known that a finite-wedge geometry leads to the possibility of multiple scattering from the two broad interfaces, as well as the sides of the structure. Therefore, the main issue is how to choose the correct beam containing the right information about the rightness of the PC from the multiple scattering beams out of the wedge. Thus the determination of the right design for the wedge as well as attributing the correct rightness to the outgoing beam is of crucial importance in such kind of experience.

4.2.1 Wedge structure

In this part we theoretically and experimentally study the negative refraction in a 2D wedge shaped PC. The structure consists of a triangular array of ceramic rods of a dielectric constant 9.61 in air, see Fig. 4.12. The rods have a length of $l = 15cm$

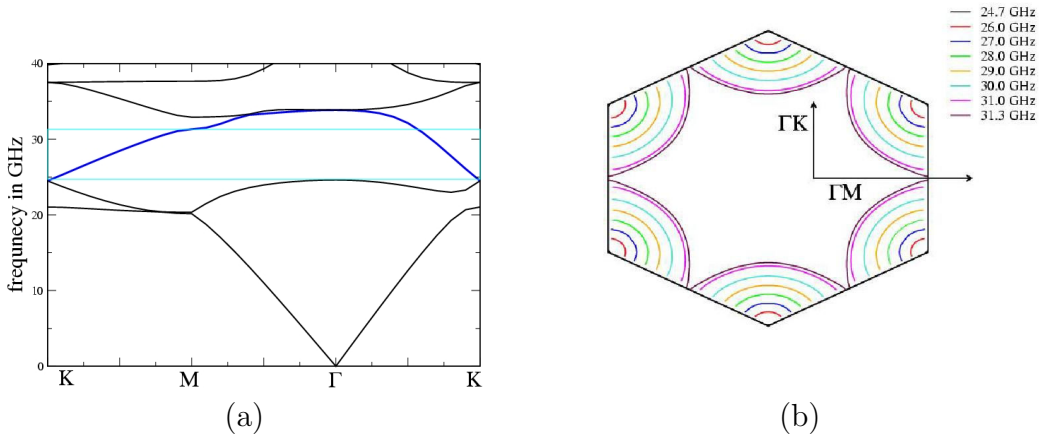

(a) (b)

Figure 4.13 (a) The photonic band structure for the TE- polarization with the shaded area being the area of interest in which our PC behaves as a LH. (b) The Equal Frequency Surfaces (EFS) for some selected frequencies.

and a diameter of $d = 3.182mm$. The center-to-center separation between the rods is $a = 6.343mm$ along the ΓK direction and $b = 10.99mm$ along the ΓM direction. The structure length along ΓK and ΓM is 29 and 11 layers respectively.

The plane wave method is used to compute the photonic band structure as well as the equi-frequency surfaces (EFS), which is done by S. Foteinopoulou. Some of the theoretical results are obtained using the Finite Difference Time Domain (FDTD) method by R. Moussa. This method shows a time and space evolution of the emitted EM waves. More details of this algorithm can be found in [47, 49]. In all the FDTD simulations, a perfect matching layer (PML) boundary conditions [4, 3] are used. The source emits a monochromatic TE-(H-) polarization of desired frequency. A Gaussian source (Gaussian in space and "almost" monochromatic) is placed outside the structure to check for the negative refraction. The photonic band structure as well as the EFS in $\mathbf{k}$ space are shown in Fig. 4.13. Note that the EFS consist of the allowed propagation modes for a specific frequency. The shaded region extending from 24.7 to 31.3 GHz is of particular interest. This particular region does not start at the bottom of the third band to avoid any overlapping with the second band. Since this region has $\mathbf{v_g} \cdot \mathbf{k} < 0$, where $\mathbf{v_g}$

is the group velocity. Therefore, our PC in this particular range of frequencies exhibits LH behavior. The EFS in the first Brillouin zone are anisotropic and are shown as broken curves with six-fold symmetry in **k**-space (see Fig. 4.13b). For selected frequencies in the shaded regions the curves move inwards with increasing frequency. Above 31.3 GHz, the EFS curves start to close and the phase refractive index becomes too small making the determination of the LH behavior too difficult. Therefore we restrict our region of interest up to 31.3 GHz.

4.2.2 Theoretical Calculation and experimental data

Our experimental setup consists of an HP 8510C network analyzer, a microwave horn antenna as the transmitter and another horn antenna as the receiver. The second antenna sweeps along the second interface as shown in Fig. 4.13a. The real view of the wedge can also be found in Fig. 4.15. A baffle with an aperture of 10 cm is localized at the first interface of the wedge. The distance from the first interface to the source antenna is kept at 100 cm while the second antenna sweeps around at a distance of 160 cm. The source antenna generates an incoming EM launched normally to the interface of our wedge structure. This part of measurement was in collaboration with K. Lin of Boeing Phantom Works. Both ΓK and ΓM interfaces have been studied separately. The outgoing beam is measured at all angles. Indeed, the detector sweeps from -90 deg to almost $+90$ deg.

Following the band structure, our PC at low frequencies behaves as a RH material with a positive refractive index. Indeed, the wavelength is large compared to the lattice constant and consequently, an effective medium theory can be applied. To test our setup and to get an idea if the experimental data agrees with the theory, we measured the transmission for both polarization at 8 GHz. For this test case, the EM waves were launched along ΓM and the interface was along ΓK. All angles were measured with respect to the wedge normal (see Fig. 4.14a). The transmission spectra showed

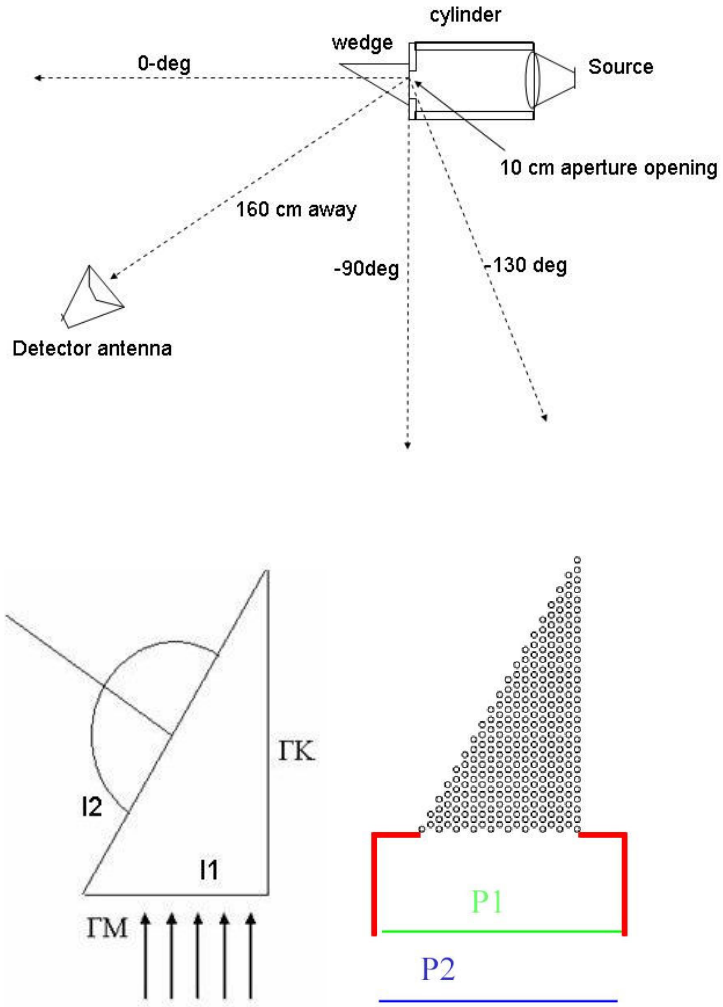

(a) (b) (c)

Figure 4.14 (a) The setup for the wedge experiment. (b) the wedge design $\Gamma M \Gamma M$ in which the EM waves are launched along ΓK. Both interface (I1) and (I2) are along the ΓM direction. The normal to (I2) divide the hemisphere to an upper and lower half. The upper half correspond to positive refraction and the lower one correspond to the negative refraction. (c) The modeled metallic baffle, the green line shows the position of the source.

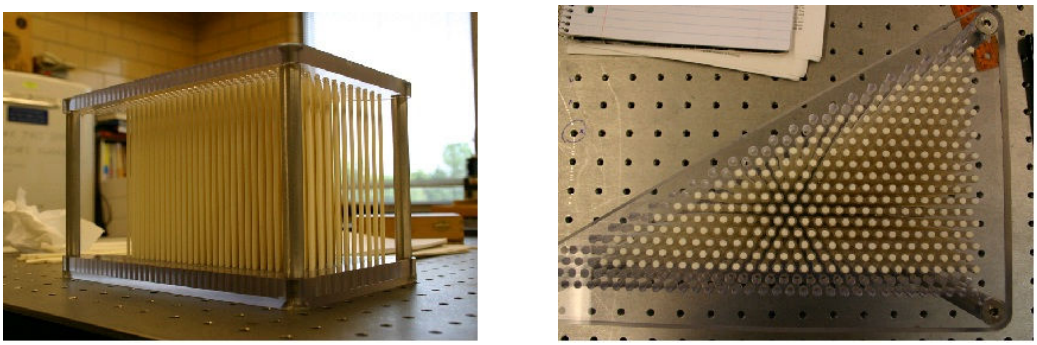

(a) (b)

Figure 4.15 Real view of the wedge structure in lab, from top and side

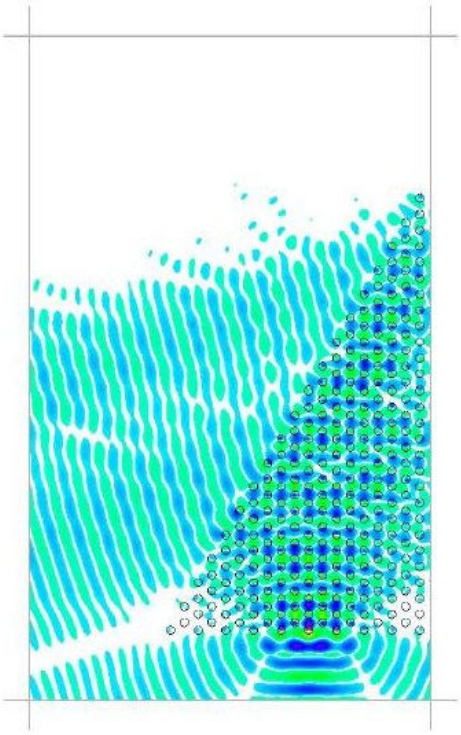

Figure 4.16 The magnetic field for the TE- polarization at a frequency of 29 GHz with the four beams b1, b2, b3, b4 arrows being the first order Bragg beam, the outgoing one, the higher order1 and the higher order2 respectively.

an outgoing angle of 41 and 56 deg for H- and E-polarizations respectively. From the effective medium theory, an effective dielectric constant of 1.45 for H-polarization and 2.95 for the E-polarization corresponding to calculated outgoing angles of 37 and 59 degrees respectively. These results indicate a good agreement between experiment and theory at low frequencies. As shown in Fig. 4.13b, the EFS plots are anisotropic with broken curves with 6-fold symmetry. This implies that higher order beams are expected making the design and the interpretation of the wedge results more difficult [29]. Due to these reasons and ambiguities arising from the comparable outgoing angles, we chose to work with $\Gamma M - \Gamma K$ design. Moreover, for $\Gamma M - \Gamma M$ design, even if the higher order beams do couple, they will not interfere with the rightness and the characterization of the LH or RH behavior of the PC. From the EFS calculation, different diffracted beams are expected. Thus, it will be difficult to assign RH or LH behavior to one of them. However, it is known that the rightness of the material is related to the large magnitude transmitted (zeroth order) outgoing beam. Fig. 4.16 shows the magnetic field at 29 GHz. Notice that for all the FDTD results, the EM waves are launched along the ΓK direction. The first and second interfaces of the wedge structure, I1 and I2 respectively are along ΓM (see Fig. 4.14b). Two larger beams are diffracted. One of them is the outgoing beam and the second one is the first order Bragg beam due to the periodicity at the second interface (I2). The other two beams are the higher order Bragg reflections at the first interface (I1) and are due to the combined effects of the periodicity of the interface (I1) and the anisotropic six-fold symmetrical EFS. To assign a LH behavior to one of the diffracted beams at the second interface (I2), it is important to be able to characterize the LH or RH nature of the propagating beams. Therefore, one has to assign a sign for the rightness of the PC. We chose that the negative hemisphere correspond to the negative refraction and the positive hemisphere correspond to the positive refraction.

Although theory (photonic band structure and EFS calculation) predicted LH behavior for the wedge PC in the frequency range of interest, experimental data showed no

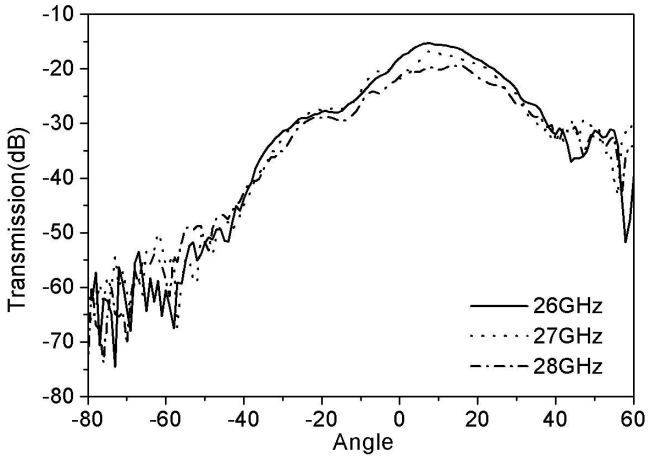

Figure 4.17 The transmission versus the angle measured from the surface normal for the three frequencies; 26, 27, 28 GHz.

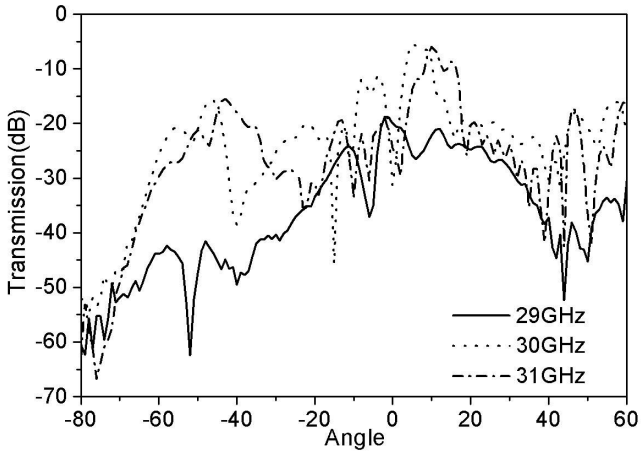

Figure 4.18 The transmission versus the angle measured from the surface normal for the three frequencies: 29, 30, 31 GHz.

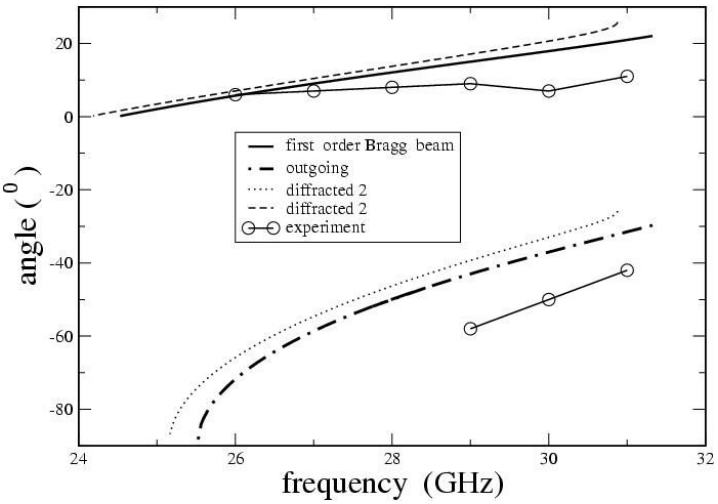

Figure 4.19 The angle in degree versus the frequency for the four possible diffracted beams in comparison with the experiment

such peak before 29 GHz. The transmission versus the measured angle from the surface normal are plotted in Fig. 4.17 and Fig. 4.18 for the ranges of 26–28 GHz and 29–31 GHz respectively. This discrepancy between theory and experiment will be addressed later. It result from the comparison between theoretical and experimental results that: From 26–28 GHz, the experimental data shows no negative peak. The only peak observed in this plot is the one corresponding to the positive refraction around 15 deg. However, starting from 19 GHz two peaks are observed. One corresponds to the negative refraction and the other one to the positive refraction. Fig. 4.19 summarizes all the possible diffracted beams from the theory as well as from the experiment. It is clearly shown that the first order Bragg peak has an angle much smaller in magnitude than the zeroth order beam. The other two higher order beams are very close to the transmitted and first order Bragg peaks. In general, the experimental data seems to fall below the theoretical ones. A good agreement between theory and experiment results concerning the position of the negative peak is found. However, a reasonable agreement is found between theory and experiment concerning the position of the positive peak. Furthermore the FDTD simulations suggested that the positive peak will have much less amplitude than the neg-

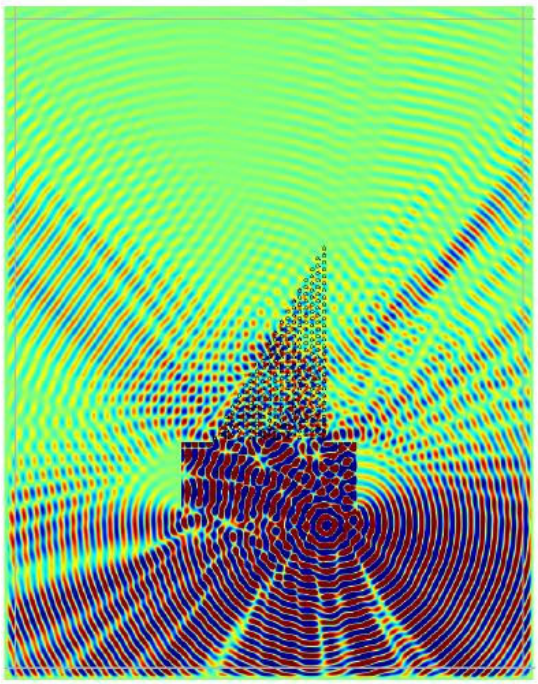

Figure 4.20 The magnetic field for the TE- polarization at a frequency of 26 GHz with the four beams b1, b2, b3, b4 arrows being the first order Bragg beam, the outgoing one, the higher order1 and the higher order2, respectively. A baffle is considered and the source is at a distance of 160cm.

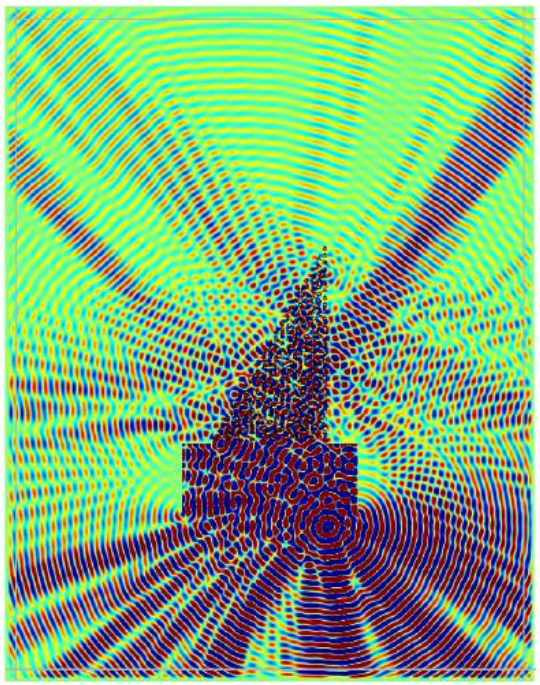

Figure 4.21 The same as Fig. 4.20 at a frequency of 30 GHz.

ative one. So far two discrepancies are present between the theory and the experiment. The first one is the absence of the negative peak between 26 GHz and 28 GHz and the second one is the magnitude of the positive peak being higher than the magnitude of the negative one. To investigate these two discrepancies, many parameters were examined. Three factors were singled out as the most likely source of the discrepancies. This include the small imperfections around the location of the scatters, the width of the source and the metallic baffle. It was found that the small imperfections make no difference and they do no effect the result. The source width slightly increases and enhances the positive peak. However, the metallic baffle appeared to be the major contributor. To investigate this effect, a Π shaped baffle modeled to emulate the experimental data was considered in the FDTD simulations. The metallic baffle was has the dimension of 0.818 mm and 0.709 mm with respect to x and y directions with an opening of approximately 10 cm. The source is collimated like Gaussian beam localized at a distance of 160cm. Fig. 4.20 and Fig. 4.21 show the FDTD results with the metallic baffle for 26 GHz and 20GHz respectively. Compared to the case where no baffle is considered, Fig. 4.21 at 30 GHz shows an enhancement of the relative magnitude of the positive peak. This explains why the positive peak has much higher magnitude compared to the negative one in the experimental data. Furthermore, although the metallic baffle does not affect the position of the outgoing peaks, it significantly influence their relative power. Particularly at 26 GHz (see Fig. 4.20), the LH peak is much weaker than the positive peak and is barely observable. This may be the reason why below 29 GHz, no negative peak was observed. One possible explanation in favor of the metallic baffle would be adding the metallic baffle, the two higher order reflections were partially suppressed and they were fed back inside the structure. Thus, the positive peak gains more power and become considerably significant.

4.2.3 Conclusion

In conclusion, we have experimentally and theoretically studied the negative refraction and all possible outgoing peaks from a wedge shaped PC in such a way that the rightness of our PC is unambiguously determined. The theory agrees very well with the experiment at lower frequencies as well as for the position of the positive and negative peak at higher frequencies. However, some discrepancies related to the magnitude of the positive and the negative peak as well as their appearance have been seen. Simulations show that the baffle may be the reason of such discrepancies.

4.3 Summary

In this chapter, we discussed the transmission properties of two-dimensional photonic crystal structures composed of dielectric materials. Negative refraction has been predicted and experimentally verified in photonic crystal structures we proposed. Superlensing phenomenon is also observed in one of the photonic band-gap structures. It has high transmission along a wide range of angles, which makes it a good candidate for observing LH behavior in PCs.

CHAPTER 5 Experimental Procedure to Test Negative Index

In this chapter we present the experimental methods involved in the course of measurements to verify the negative refractive index of left-handed materials. There are two major procedures that have been carried out in the microwave lab. The first method is to measure the magnitude and phase of transmission and reflection and inverse refractive index from the retrieval procedure explained in Chapter 2; the other method is to determine the refractive index of testing material by measuring the location of first node of standing wave.

5.1 Transmission and refection measurement

Measurements are taken using a HP 8510 network analyzer. A pair of Narda standard gain waveguide horn antennas are used as transmitter and receiver.

To obtain transmission, a slab of left-handed material sample is placed between transmitter and receiver antennas. The transmission is measured as a function of frequency and calibrated to the transmission between the horns with the sample removed.

The reflection measurements is taken by placing the transmitter and receiver horns on the same side of the sample and bouncing the microwave signal off the sample. The pair of antennas are each inclined with an very small angle (about 7°) with respect to normal on the sample surface. The reflection measurement is calibrated using a sample-sized sheet of copper as a reflecting mirror, see Fig. 5.1.

The transmission and reflection results then can be used to extract the effective refractive index.

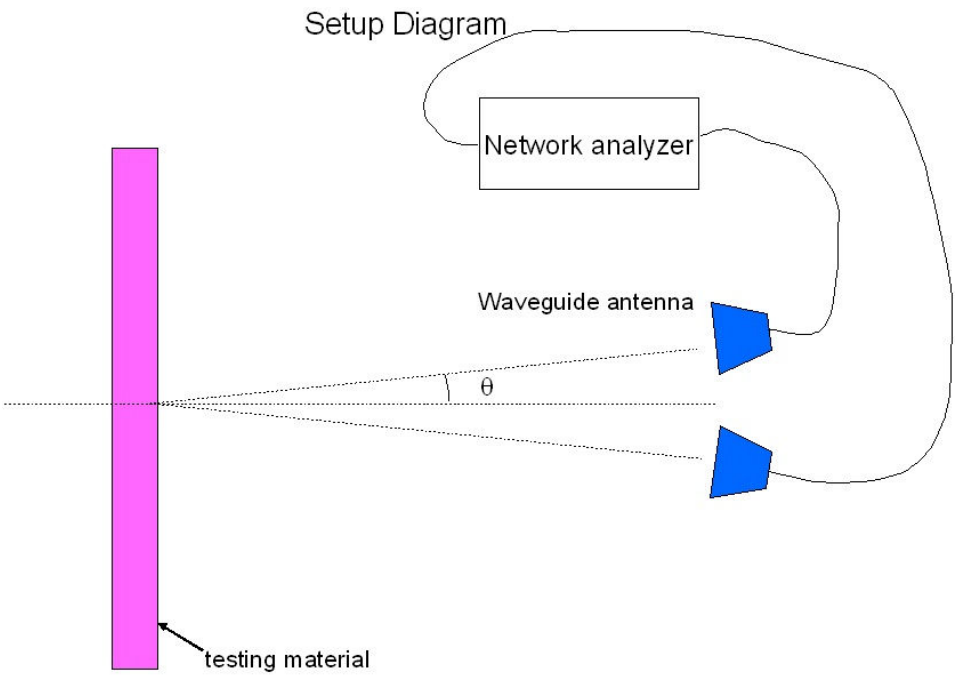

Figure 5.1 Reflections measurement setup, both source and receiving antennas are tilted at a small angle

5.2 First node detection

Fig. 5.2 shows the experiment setup used to observe standing waves in free space. The dipole antenna is controlled by a Klinger gear motor connected by a motor controller/driver and moved away from the slab of sample. The horn antenna generates electromagnetic wave and the wave is reflected back from the metallic mirror. Its reflected wave interferences with the incident wave and a standing wave pattern appears. The dipole antenna detects the superposition of both incident and reflected wave and the E field will be recorded as well as the positions. A node is a position where the amplitude of the stationary wave is zero and the first node appears at the position of half wavelength away from reflector.

We test 12.7 mm-thick rexolite slab in the lab. The standing wave pattern is given in Fig. 5.3.

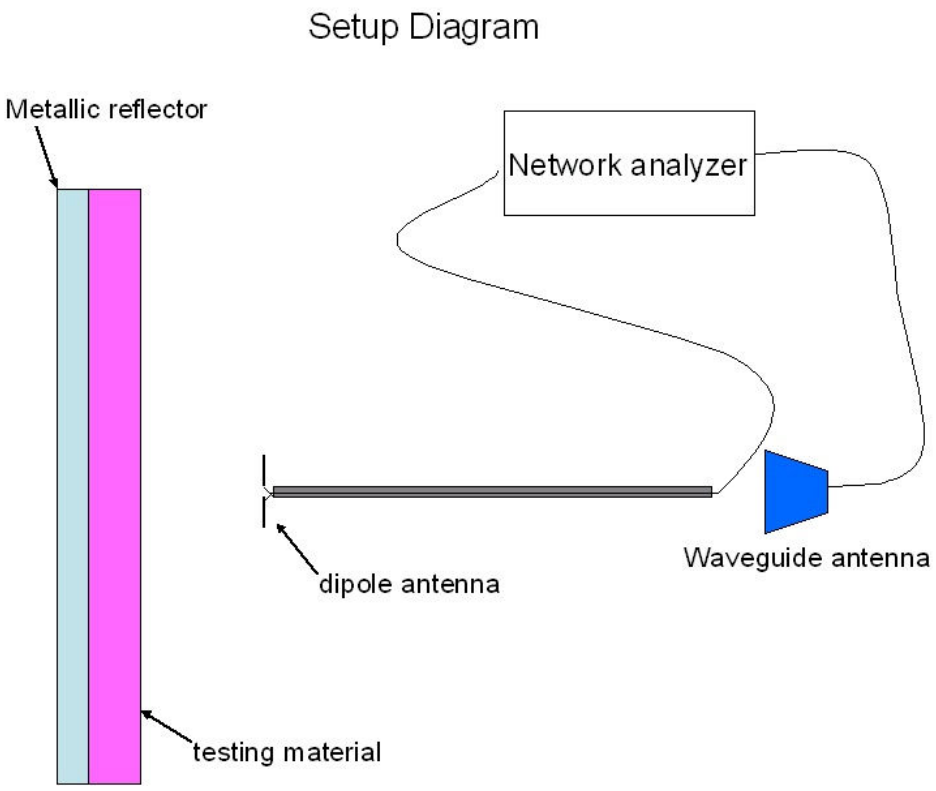

Figure 5.2 Index determination by locating the first node of standing wave.

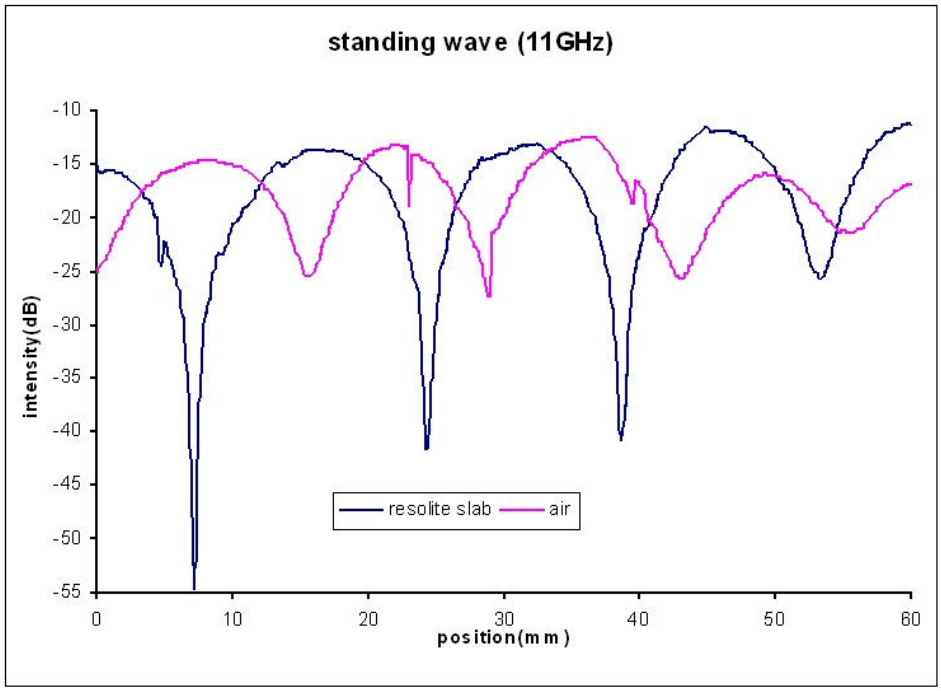

Figure 5.3 Standing wave pattern for a piece of rexolite slab

The first nodes is located 7.2 mm away from the rexolite slab, so we have:

$$7.2mm + n * 12.7mm = \lambda/2, \tag{5.1}$$

where n is the refractive index of the rexolite slab. $n = 1.58$ is calculated from (5.1) while $n = 1.59$ from manufacturer's catalog, they are very close. We noticed that the first node moves closer to the metallic mirror when there is rexolite slab than without. That is due to the refractive index of rexolite is greater than the one of air. If a negative index material is placed in front of the metallic mirror, the first is moving further away from the reflector. From locating the first node of standing wave, the refractive index can be obtained experimentally.

BIBLIOGRAPHY

[1] K. Aydin, K. Guven, M. Kafesaki, L. Zhang, C. M. Soukoulis, and E. Ozbay. Experimental observation of true left-handed transmission peaks in metamaterials. *Opt. Lett*, 29:2623–2625, 2004.

[2] M. Bayindir, K. Aydin, E. Oabay, P. Markos, and C. M. Soukoulis. Transmission properties of composite metamaterials in free space. *Appl. Phys. Lett*, 81:120–122, 2002.

[3] J.-P. Berenger. Perfectly matched layer for the FDTD solution of wave-structure interaction problems. *IEEE Transactions on Antennas and Propagation*, 44(1):110–117, January 1996.

[4] Jean-Pierre Berenger. A perfectly matched layer for the absorption of electromagnetic waves. *Journal of Computational Physics*, 114(2):185–200, October 1994.

[5] E. Cubukcu, K. Aydin, E. Ozbay, S. Foteinopolou, and C. M. Soukoulis. Subwavelength resolution in a two-diemnsional photonic-crystal-based superlens. *Phys. Rev. Lett*, 91:207401–4, 2003.

[6] C. Enkrich, S. Linden, M. Wegener, S. Burger, L. Zswchiedrich, F. Schmidt, J. Zhou, T. Koschny, and C. M. Soukoulis. Magnetic metamaterials at telecommunication and visible frequencies. *Phys. Rev. Lett*, 95:203901, 2005.

[7] S. Foteinopoulou, E. N. Economou, and C. M. Soukoulis. Refraction in media with a negative refractive index. *Phys. Rev. Lett*, 90:107402–4, 2003.

[8] S. Foteinopoulou and C. M. Soukoulis. Negative refraction and left-handed behavior in two-dimensional photonic crystals. *Phys. Rev. B*, 67(23):235107, Jun 2003.

[9] S. Foteinopoulou and C. M. Soukoulis. Em wave propagation in two-dimensional photonic crystals: a study of anomalous refractive effects. *cond-mat/0403542*, 2004.

[10] S. Foteinopoulou and C. M. Soukoulis. Electromagnetic wave propagation in two-dimensional photonic crystals. *Physical Review B*, 72(16), 2005.

[11] N. Garcia and M. Nieto. Left-handed materials do not make a perfect lens. *Phys. Rev. Lett*, 88:207403, 2002.

[12] P. Gay-Balmaz, J.F., and J. Martin Olivier. Electromagnetic resonances in individual and coupled split-ring resonators. *Appl. Phys.*, 92:2929, 2002.

[13] G. Hooft. Comment on 'negative refraction makes a perfect lens'. *Phys. Rev. Lett*, 87:249701, 2001.

[14] A. A. Houck, J. B. Brock, and I. L. Chuang. Experimental observations of a left-handed material that obeys snell's law. *Phys. Rev. Lett.*, 90:137401–4, 2003.

[15] N. Katsarakis, T. Koschny, M. Kafesaki, E.N. Economou, and C.M. Soukoulis. Electric coupling to the magnetic resonance of split ring resonators. *Appl. Phys. Lett.*, 84:2943, 2004.

[16] H. Kosaka, T. Kawashima, A. Tomita, M. Notomi, T. Tamamura, T. Sato, and S. Kawakami. Superprism phenomena in photonic crystals. *Phys. Rev. B*, 58:10096–99, 1998.

[17] T. Koschny, M. Kafesaki, E. N. Economou, and C. M. Soukoulis. Effective medium theory of left-handed materials. *Phys. Rev. lett*, 93:107402–4, 2004.

[18] T. Koschny, P. Markos, D. R. Smith, and C. M. Soukoulis. Resonant and antiresonant frequency dependence of effective parameters of metamaterials. *Phys. Rev. E*, 68:65602–4, 2003.

[19] Th. Koschny, P. Markos, E. N. Economou, D. R. Smith, D. C. Vier, and C. M. Soukoulis. Impact of the inherent periodic structure on the effective medium description of left-handed and related meta-materials. *Phys. Rev. B*, 71:245105, 2005.

[20] K. Li, S.J. McLean, R.B. Gregor, C.G. Parazzoli, and M. Tanielian. Free-space focused-beam characterization of left-handed materials. *Appl. Phys. Lett*, 82:2535, 2003.

[21] Z. P. Liao, H. L. Wong, B. P. Yang, and Y. F. Yuan. A transmitting boundary for transient wave analysis. *Sci. Sin., Ser.A*, 27:1063–1076, 1984.

[22] R. Liu, A. Degiron, J. J. Mock, and D. R. Smith. Negative index material composed of electric and magnetic resonators. *Applied Physics Letters*, (to appear).

[23] C. Luo, S. G. Johnson, J. D. Joannopoulos, and J. B. Pendry. Al-angle negative refraction without negative effective index. *Phys. Rev. B*, 65:201104, 2002.

[24] P. Markos, I. Rousochatzakis, and C. M. Soukoulis. Transmission losses in left-handed material. *Phys. Rev. E*, 66:107402–4, 2002.

[25] P. Markos and C. M. Soukoulis. Numerical studies of left-handed materials and arrays of split ring resonators. *Phys. Rev. E*, 65:036622–8, 2002.

[26] P. Markos and C. M. Soukoulis. Transmission studies of left-handed materials. *Phys. Rev. B*, 65:033401–4, 2002.

[27] P. Markos and C. M. Soukoulis. Absorption losses in periodic arrays of thin metallic wires. *Opt. Lett*, 28:846–848, 2003.

[28] R. Marques, F. Medina, and R. Rafii-El-Idrissi. Role of bianisotropy in. negative permeability and left-handed metamaterials. *Phys. Rev. B*, 65:44440, 2002.

[29] M. Notomi. Theory of light propagation in strongly modulated photonic crystals: Refractionlike behavior in the vicinity of the photonic band gap. *Physical Review B*, 62(16):10696+, October 2000.

[30] E. Ozbay, K. Aydin, E. Cubukcu, and M. Bayindir. Transmission and reflection properties of composite double negative metamaterials in free space. *IEEE Trans. on Antennas and Propagation*, 51:2592, 2003.

[31] J. Pacheco, T. M. Grzegorczyk, B. I. Wu, Y. Zhang, and J. A. Kong. Power propagation in homogeneous isotropic frequency-dispersive left-handed media. *Phys. Rev. Lett.*, 89:257401–04, 2002.

[32] C. G. Parazzoli, R. B. Gregor, K. Li, B. E. C. Koltenbah, and M. Tanielian. Experimental verification and simulation of negative index of refraction using snell's law. *Phys. Rev. Lett*, 90:107401–4, 2003.

[33] J. B. Pendry. Negative refraction makes a perfect lens. *Physical Review Letters*, 85(18):3966+, October 2000.

[34] J. B. Pendry, A. J. Holden, W. J. Stewart, and I. Yongs. Extremely low frequency plasmons in metallic mesostructures. *Phys. Rev. Lett*, 76:4773–4776, 1996.

[35] J. B. Pendry, A. J. Holden, W. J. Stewart, and I. Yongs. Magnetism from conductors and enhanced nonlinear phenomena. *IEEE Trans. Microw. Theory Tech*, 47:2075–2084, 1999.

[36] V. A. Podolskiy and E.E. Narimanov. Near-sighted perfect lens. *Opt. Lett.*, 30:75–77, 2005.

[37] D. R.Smith, S. Schultz, P. Markos, and C. M. Soukoulis. Determinations of effective permittivity and permeability of metamaterials from reflection and transmission coefficients. *Phys. Rev. B*, 65:195104–5, 2003.

[38] R. Ruppin. Electromagnetic energy density in a disoersive and absorptive material. *Phys. Lett. A*, 299, 2002.

[39] D. Schurig, J. J. Mock, B. J. Justice, S. A. Cummer, J. B. Pendry, A. F. Starr, and D. R. Smith. Metamaterial electromagnetic cloak at microwave frequencies. *Science*, 314:977–980, 2006.

[40] R. A. Shelby, D. R. Smith, S. C. Nemat Nasser, and S. Schultz. Microwave transmission through a two-dimensional, isotropic, left-handed metamaterial. *Appl. Phys. Lett*, 78:489–491, 2001.

[41] R. A. Shelby, D. R. Smith, and S. Schultz. Experimental verification of a negative index of refraction. *Science*, 292:77–79, 2001.

[42] Mario Silveirinha and Nader Engheta. Tunneling of electromagnetic energy through subwavelength channels and bends using epsilon-near-zero materials. *Physical Review Letters*, 97(15):157403, 2006.

[43] D. R. Smith, W. J. Padilla, D. C. Vier, S. C. Nemat Nasser, and S. Schultz. Composite medium with simultaneously negative permeability and permittivity. *Phys. Rev. Lett*, 84:4184–4187, 2000.

[44] D. R. Smith, S. Schultz, P. Markos, and C. M. Soukoulis. Determination of effective permittivity and permeability of metamaterials from reflection and transmission coefficients. *Phys. Rev. B*, 65:195104–5, 2002.

[45] D. R. Smith, D. C. Vier, Th. Koschny, and C. M. Soukoulis. Electromagnetic parameter retrieval from inhomogeneous metamaterials. *Phys. Rev. E*, 71:121103, 2005.

[46] D. R. Smith, D. C. Vier, N. Kroll, and S. Schultz. Direct calculation of permeability and permittivity for a left-handed metamaterial. *Appl. Phys. Lett*, 77:22462248, 2000.

[47] A. Taflove. Computational electrodynamics-the finite difference time-domain method. *Artech House*, 1995.

[48] V. Veselago. The electrodynamics of substances with simutaneously negative values of epsilon and mu. *Phys. Usp.*, 1968.

[49] Kane Yee. Numerical solution of inital boundary value problems involving maxwell's equations in isotropic media. *IEEE Transactions on Antennas and Propagation*, 14(3):302–307, March 1966.

[50] Lei Zhang, G. Tuttle, and C. M. Soukoulis. Ghz magnetic response of split ring resonators. *Photonic and Nanostructures*, 2:155, 2004.